Exploring Properties of MoS_2 Transferred Onto Periodically Patterned Substrates.

Alexandre Imbert

Thesis submitted to the University of Ottawa in partial fulfillment of the requirements for the Master of Science Physics

Department of Physics.

Faculty of Science.

University of Ottawa

Contents

Acknowledgement

I would like to express my sincere gratitude to Professor Adina Luican-Mayer for her guidance, support, and insight over the course of the project; her drive continues to inspire me.

I would also like to thank all the members of the Luican-Mayer laboratory for their camaraderie and valuable discussions that helped me over the years.

I would like to thank the nanoFAB at the University of Alberta and Professor Mathieu de Lafontaine for the manufacturing of the photomask.

I would like to thank my friends and my parents for encouraging my curiosity from a young age and allowing me to pursue my passion.

Finally, a huge thank you to Mutahir Butt for his words of encouragement and his unwavering support.

Abstract

This project aimed to characterize the strain in few-layer MoS_2 via Raman spectroscopy. Periodic patterns were etched into Si/SiO_2 wafers using photolithography, after which MoS_2 flakes were exfoliated and transferred on top of the patterns, leading to a mechanical deformation of the layers. We investigated the topography of the flakes via atomic force microscopy, and discovered that the sudden drop-off of the flakes had led to an increased presence of air bubbles. By investigating our samples with Raman spectroscopy, we first confirmed the presence of the two characteristic peaks E^1_{2g} and A_{1g}. Comparison with other studies indicates that our MoS_2 flakes are thinner than our AFM measurements suggested, which we attribute to presence of air bubbles, which can both artificially increase the step heights as well as disturb the vibrational modes. Modulations in the Raman response around the location of the bubbles shows a softening of the difference of the peak position, although the change is not significant enough. Similarly, no significant change in the Raman response was observed at the edges of the patterns, due to the shallow etch depth, which does not induce a strain important enough to be resolved by our Raman system. These results highlight the challenges associated with strain characterization of crystalline systems.

Chapter 1

Introduction

1.1 2D materials and transition metal dichalcogenides

Two-dimensional (2D) materials first garnered interest with the isolation of graphene in 2004 [1], showcasing that stable atomically thin crystals could be mechanically exfoliated from their bulk counterparts. This breakthrough revealed a new realm of van der Waals-bonded layered systems whose properties diverge dramatically from those in three dimensions, leading to research into a wide variety of 2D compounds. Beyond graphene's semimetallic behaviour, the 2D materials family features compounds such as insulators (h-BN), metals (TiS_2), superconductors ($RbSe_2$) and semiconductors such as the transition metal dichalcogenides (TMDs) family. [2–6]. TMDs are a class of 2D materials with a stoichiometry of MX_2, where M represents transition metal atoms and X represents chalcogen atoms, as illustrated in Figure 1. The strong in-plane covalent bonds and the weak out-of-plane van der Waals interactions enable the isolation of single or few layers of 2D materials without compromising the in-plane lattice.

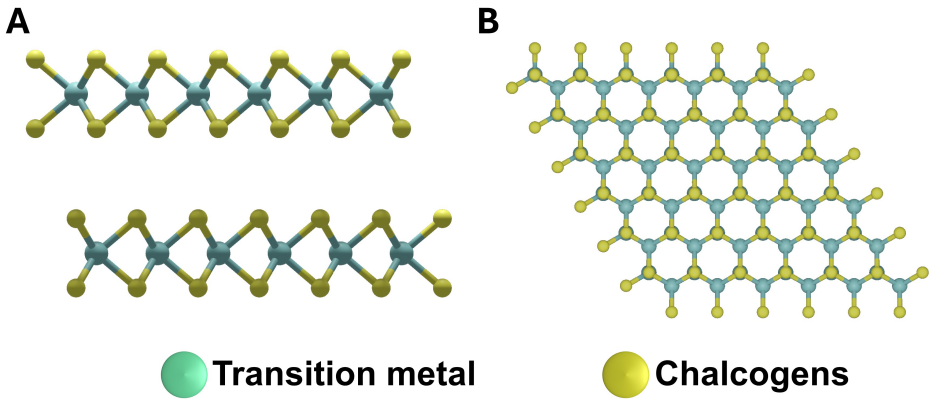

Figure 1: A) Side and B) top view representations of a TMD.

1.2 Electronic and optical properties of semiconducting TMDs

This strong in-plane covalent bonds lead to TMDs exhibiting extreme mechanical flexibility [7–10] while their reduced dimensionality makes them especially sensitive to mechanical deformations. Molybdenum Disulfide (MoS_2) is one of the most studied TMDs, due to its advantageous optical properties and availability. MoS_2, like other TMD monolayers, exhibits an indirect bandgap of ∼1.2 eV in its bulk form, whereas when thinned down to a monolayer, it transitions to a direct bandgap of ∼1.9 eV [11–14], as shown by black arrows in Figure 2. This transition dramatically enhances its photoluminescence efficiency, making monolayer MoS_2 highly attractive for optoelectronic applications such as photodetectors [15], light-emitting diodes, and solar cells. Monolayer TMDs are particularly intriguing due to their strong spin-orbit coupling (SOC), a phenomena in which the interaction between an electron's spin and its orbital momentum lifts the spin degeneracy of the bands at the K and K points. **references**. Combined with the lack of inversion symmetry, leading to the different K valleys being inequivalent, this ties the spin to the valley, which is known as spin-valley locking. This coupling enables valley-selective optical transitions using circularly polarized

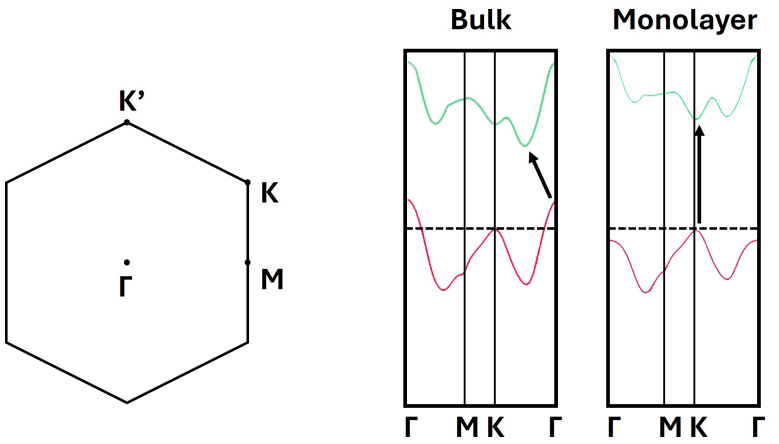

Figure 2: Band structure comparison of bulk and monolayer MoS_2 [14]

light, introducing a pseudospin degree of freedom that can be harnessed for valleytronic and spintronic applications. The reduced dimensionality in thin systems also leads to tightly bound excitons with large binding energies, further enhancing light–matter interactions [16–20]. Recent advances in synthesis techniques, including chemical vapor deposition (CVD) and molecular beam epitaxy (MBE), have enabled the scalable production of high-quality monolayers with controlled thickness, crystallinity, and domain orientation. These developments are critical for integrating semiconducting TMDs into next-generation flexible, transparent, and energy-efficient electronic and photonic devices.

1.3 Motivation – Engineering 2D materials using periodic substrates

The properties of semiconducting 2D materials can be engineered not only through intrinsic factors such as thickness and composition, but also by carefully designing their interaction with underlying substrates. In particular, periodic substrates—those patterned with nanoscale or microscale periodicities offer a versatile route to modulate

structural, electronic, and optical responses of 2D layers. The periodic potential imposed by the substrate can couple to the lattice of the 2D material, leading to effects such as strain modulation, band structure reconstruction, and the emergence of moiré superlattices. For example, when the periodicity of the substrate is commensurate or nearly commensurate with the lattice constant of the 2D material, new minibands can form, altering carrier mobility, exciton dynamics, and valley polarization. Engineering across different periodicity regimes allows tuning of both fundamental properties and device-level performance. For instance, nanoscale periodicities can be exploited to confine excitons or modify phonon dispersion, while microscale patterns can enhance light extraction or guide plasmonic modes.

In this project, we transferred MoS_2 onto periodic patterns we etched in the substrates. These patterns were realized via photolitography, which replicates desired geometries etched into a reusable photomask. Although the periodic nature of the patterns is not probed in the project, another use that comes to mind for our designed photomask is to periodically pattern the gates of a structure to probe new regimes and modulate the behaviour of charge carriers in 2D.

1.3.1 Modulating electronic properties with periodic gates

Unlike uniform gating, where a global back gate or top gate applies the same electrostatic field across an entire device, periodic gating introduces a spatially varying potential landscape. By patterning gate electrodes with periodicities ranging from a few nanometers to several hundreds of nanometers, one can create alternating regions of high and low carrier density, effectively engineering artificial superlattices. This engineered potential landscape is conceptually similar to that arising in moiré systems, where long-range interference patterns form due to small lattice mismatches or twist angles between stacked atomic layers. In both cases, the periodic modulation can give rise to miniband formation, altered density of states, and localization of carriers in potential wells. A critical parameter is the gate voltage amplitude, which determines

the depth of the potential modulation and the degree to which the electronic band structure is reshaped. By tuning the gate amplitude and periodicity, one can induce phenomena such as bandgap renormalization, flat-band formation, and modulation of excitonic resonances.

Research on moiré systems—often referred to as twistronics—has already revealed unconventional superconductivity, correlated insulating phases, and topologically nontrivial states [21–27]. Periodic gating offers a complementary and more controllable approach to achieving similar physics. Unlike traditional moiré heterostructures, which require precise stacking and twist-angle control, periodic gating can be applied to single-layer materials. Moreover, the effective "twist angle" or modulation strength can be continuously tuned in situ by adjusting the gate voltage, while the geometry and symmetry of the gating array (e.g., square, triangular, or 1D trenches) can be freely designed during fabrication. This flexibility makes periodic gating a promising platform for exploring correlated states, band topology, and tunable quantum phases in 2D materials. The relevant length scales of periodic gating span multiple regimes. At the nanoscale (10–50 nm), periodic potentials can directly couple to the electronic wavelength of carriers in semiconducting TMDs, leading to miniband formation and modified transport and are relevant for moiré patterns and strain superlattices. At intermediate scales (50–200 nm), periodic strain or electrostatic modulation can influence exciton localization and collective modes. At the microscale (0.5–5 µm), patterned gates can act as optical gratings, enhancing light–matter interactions and enabling spatial control of emission. Periodic gating provide a powerful and highly tunable method to engineer the electronic properties of 2D materials. By offering control over amplitude, periodicity, and symmetry, it enables the emulation of moiré potentials in single-layer systems, while also extending beyond them by allowing real-time tunability and custom-designed geometries. This approach opens new opportunities for exploring correlated electron physics, valleytronic phenomena, and optoelectronic functionalities in atomically thin semiconductors.

1.3.2 Introducing strain in 2D materials with periodic patterns

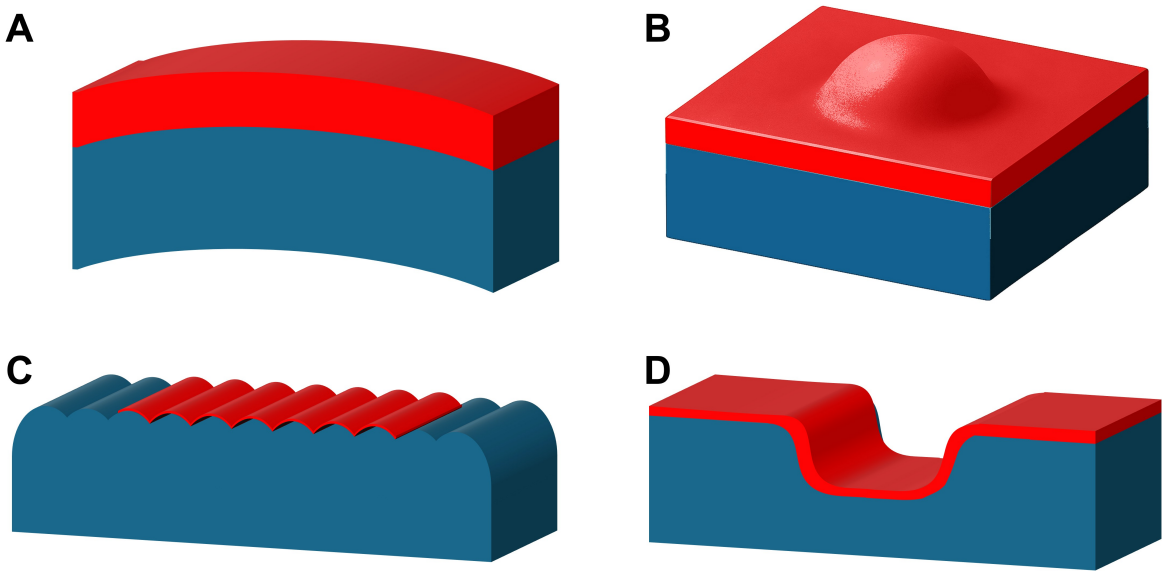

Figure 3: Schematics of common strained 2D materials systems.
A) Flexible substrate, B) trapped air bubbles, C) wrinkled substrates, D) patterned substrates

Another use of these periodic patterns is the possibility to exploit the opto-mechanical properties of 2D materials with strain engineering, which relies on stressing the materials to induce lattice deformations, modifying the interatomic distances and bond angle which directly affects their electronic properties. Strain engineering has been widely used to modify the optoelectronic [28–43], magnetic [44–47] and electrochemical [48,49] properties of 2D materials. Strain engineering 2D materials has led to advances in single-photon emitters and solar cells [37, 40, 50–53], high stability qubits [54, 55], and is opening up pathways towards superconductivity [56–58]. Over the years, multiple techniques have been employed to induce strain in 2D materials: flexible or stretchable systems - illustrated in Figure3 A) - such as those described in [29, 38, 42, 59–61] allow for precise control of a homogeneous uniaxial strain over the device. This method is

particularly effective for studying strain-dependant properties in a controlled and tunable manner. Bubbles, caused by interfacial gases trapped during the transfer or growth processes, introduce out-of-plane deformations and act as sources of local biaxial strain in 2D materials [36, 37, 53, 62–66]. The strain magnitude and symmetry depend on the bubble size and the pressure, often resulting in radially symmetric strain fields that can significantly alter the vibrational and electronic properties. Nano-scale features, such as wrinkles, folds, or nanopillars, lead to more complex and spatially varying strain profiles. Wrinkles and folds typically induce alternating regions of compressive and tensile strain along their axis, while nanopillars can generate localized tensile strain at the apex and compressive strain around the base due to the curvature and adhesion forces [41, 45, 46, 67, 68]. Another approach is to pattern the substrates on which the crystals lie. By patterning features such as trenches, wells, pyramids, or domes, desired strain landscapes can be achieved. Sharp-edge features like trenches can produce uniaxial strain by forcing the monolayer to conform, while curved geometries like domes lead to biaxial tensile strain at the peak and compressive strain near the edges. Patterning has the advantage of allowing for more precise control both of the nature and magnitude of the strain and was exploited in this project to study the effect of patterned substrates on the vibrational response of MoS_2, which we investigated via Raman spectroscopy.

1.3.3 Characterization techniques for probing properties of 2D materials

To fully capture the properties of 2D materials, several characterization methods are used. Atomic force microscopy (AFM) and scanning tunneling microscopy (STM) provide direct visualization of surface topography and moiré patterns. Raman spectroscopy and photoluminescence (PL) mapping are widely used to quantify strain distributions, bandgap shifts, and excitonic responses. Angle-resolved photoemission spectroscopy (ARPES) can directly reveal band structure modifications and miniband formation. Transmission electron microscopy (TEM) enables structural analysis of lattice align-

ment and periodicity. Complementary electrical transport measurement provide insight into mobility modulation and carrier scattering induced by substrate periodicity. This project used AFM and Raman spectroscopy to investigate the strained nature of our materials and are further detailed below.

Atomic force microscopy (AFM)

Unlike optical or electron microscopes, atomic force microscopy (AFM) operates by scanning an atomically sharp tip mounted on a flexible cantilever across a surface. Interatomic forces like the van der Waals interaction, repulsive contact forces, and electrostatic interaction allow AFM to produce high-resolution topographical maps of surfaces with sub-nanometer precision [69–71]. Figure 4 shows a schematic of an AFM: a LASER source is focused on the back of the cantilever and reflected into a position-sensitive photodetector. A feedback loop constantly monitors the tip-sample force during the raster. AFMs can operate in contact mode, where the tip is continuously in contact with the sample, or in tapping mode, where the tip oscillates near its resonance frequency, which lowers the risk of damaging the sample.

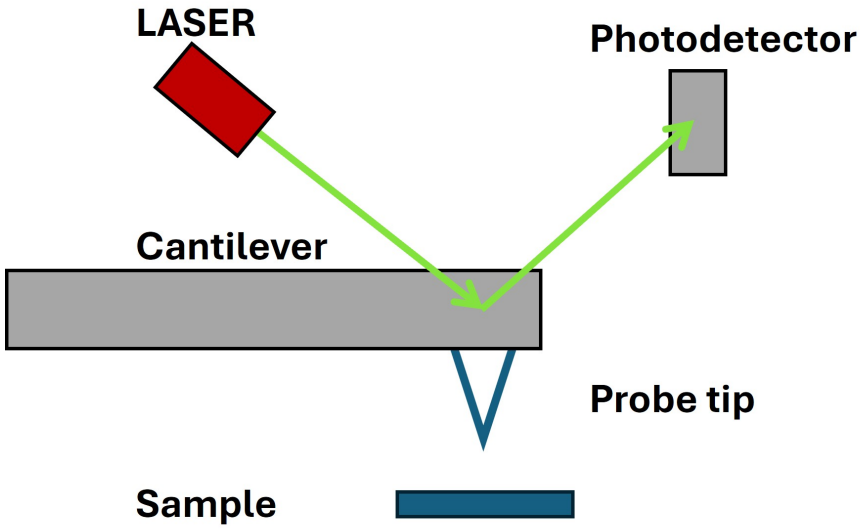

Figure 4: Schematics of an AFM

Raman spectroscopy of 2D materials

To investigate the vibrational properties of 2D materials, Raman spectroscopy serves as a fast, non-invasive and high resolution tool to characterize the structural and electronic information of 2D materials and has been used to study extensively their properties, like their number of layers [32, 60, 72–76], their level of doping [66, 77, 78] as well as any strain effects [31, 33, 38, 41–43, 59, 60, 66, 67, 76, 77].

Atoms in a crystal vibrate collectively as quantized lattice waves called phonons. In 2D materials, these phonons modes are especially sensitive to layer thickness, dielectric environment and mechanical deformation. When monochromatic light illuminates a sample, photons create an electron-hole pair, which interacts with the crystal lattice. Most scatterings are elastic, leading to a recombination of the pair and the emission of a photon with equal energy, a process known as Rayleigh scattering. A small fraction (10^{-7}) of the scatterings are inelastic: the interaction between the electron-hole pair and the lattice leads to the creation or annihilation of a phonon. The recombination of the pair leads to a photon of different energy than the incident one: in the case where a phonon is created, the emitted photon will be of lower energy (red-shifted), known as Stokes scattering. In the case of a phonon annihilation, the emitted photon will be of higher energy (blue-shifted), known as anti-Stokes scattering. [79]

$$\hbar\omega_i = \hbar\omega_s \pm \hbar\omega_p \tag{1.1}$$

Where ω_i is the frequency of the incident photon, ω_s the frequency of the scattered photon and ω_p the frequency of the phonon.

Raman spectroscopy consists of observing these energy shifts of the reemitted photons to yield a spectrum plotting the intensity of the signal as a function of the shift of energy (measured in cm^{-1}). The spectra feature a background component as well as peaks corresponding to vibrational modes indicative of the nature of the material.

In the case of bulk MoS_2, the unit cell is made of 6 atoms, therefore leading to a phonon dispersion relation exhibiting 3 acoustic and 15 optical branches. At the Γ-point, the normal phonon vibrational modes are [80–82]:

$$\Gamma = A_{1g} \oplus 2A_{2u} \oplus B_{1u} \oplus 2B_{2g} \oplus E_{1g} \oplus 2E_{1u} \oplus E_{2u} \oplus 2E_{2g} \tag{1.2}$$

Out of these 15 modes, only 4 of them are Raman active [83]: the E_{1g} mode, the two E_{2g} modes and A_{1g}. The E^2_{2g} corresponds to a shear mode and has a peak located at a low frequency of $\approx 26\text{cm}^{-1}$, which makes it difficult to isolate from the Rayleigh scattered photons. In the typical back-scattering Raman setup, the E_{1g} mode is forbidden [72,83]. The E^1_{2g} mode, whose peak is centered near 386 cm^{-1}, corresponds to the in-plane vibration of Mo and S atoms, while the A_{1g} mode, centered at approximately 405 cm^{-1}, represents the out-of-plane vibrations of S atoms. All four modes are shown in Figure 5.

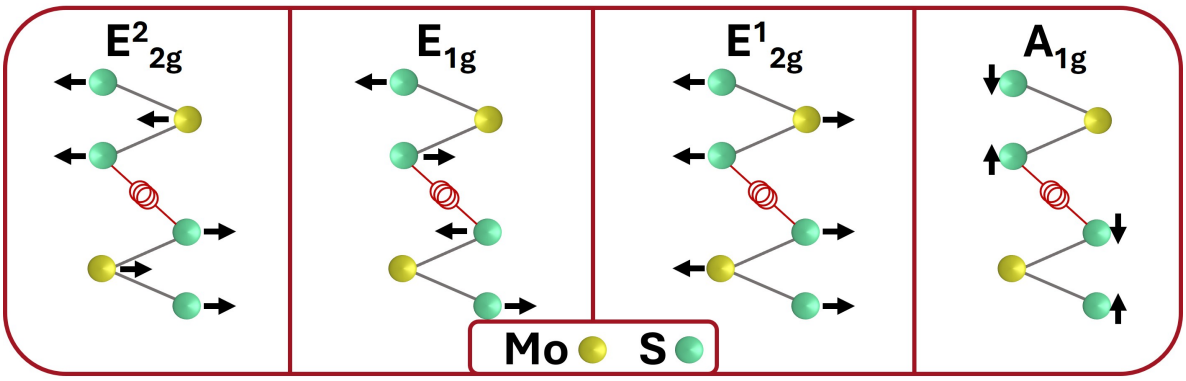

Figure 5: The four Raman active modes of MoS_2.
The red springs represent the weak interlayer force between adjacent layers.

The frequencies associated with these modes depend on the number of layers: interlayer forces (like the van der Waals force which binds the layers together) increase the effective restoring force on atoms (visualized by the red springs between S atoms in Figure 5), leading to an increase in the Raman shift for thicker MoS_2. One could thus expect

both the E^1_{2g} and A_{1g} peak positions to blue-shift with the number of layers, however it has been widely reported [32, 60, 72–75] that the E^1_{2g} peak position decreases with the number of layers. That behaviour has been attributed to possible structural changes or an increase in the long-range Coulombic interlayer interactions

Strain perturbs the restoring forces that define the phonon frequencies associated with these vibrational modes: in MoS_2, uniaxial compressive strain leads to a shrinking of the bond lengths, meaning that the wavelength of the phonons from Raman scatterings will be lower, leading to a blue-shift of the E^1_{2g} and A_{1g} peak positions. Similarly, uniaxial tensile strain manifests itself through an increase of the phonon wavelength, leading to a red-shift of the peak positions. [38, 62, 84]. Uniaxial tensile strain has also been observe to lift the degeneracy of the E^1_{2g} mode [59, 84], showing that strain can be used to disturb the symmetries of these systems. Biaxial strain has been observed to soften the modes of MoS_2 but no breaking was observed due to equibiaxial strain preserving symmetries of the system. [65]. One of the most interesting uses of strain is to modify the band gap of TMDs, which can cause a transition from a direct to an indirect bandgap in MoS_2 [59, 65, 84, 85]. These spectral shifts are not only diagnostic of the strain type and magnitude but also enable quantitative mapping of mechanical deformation across devices, making Raman spectroscopy an indispensable tool for strain engineering in 2D materials.

Figure 6 shows the different components of a Raman setup. A LASER source illuminates the sample and the reflected light is passed through an optical filter, which only lets through the Raman-scattered photons. A spectrograph then scatters the photons according to their wavelength, which are collected by a CCD detector. The Raman spectrum is obtained by plotting the intensity of the inelastically scattered light as a function of the frequency shift (Raman shift), expressed in wavenumbers (cm^{-1}). The positions, amplitudes, and linewidths of the Raman peaks are characteristic of the material's vibrational modes and are sensitive to factors such as its chemical composition, crystal structure, defects, doping, and, importantly in the context of this project, strain.

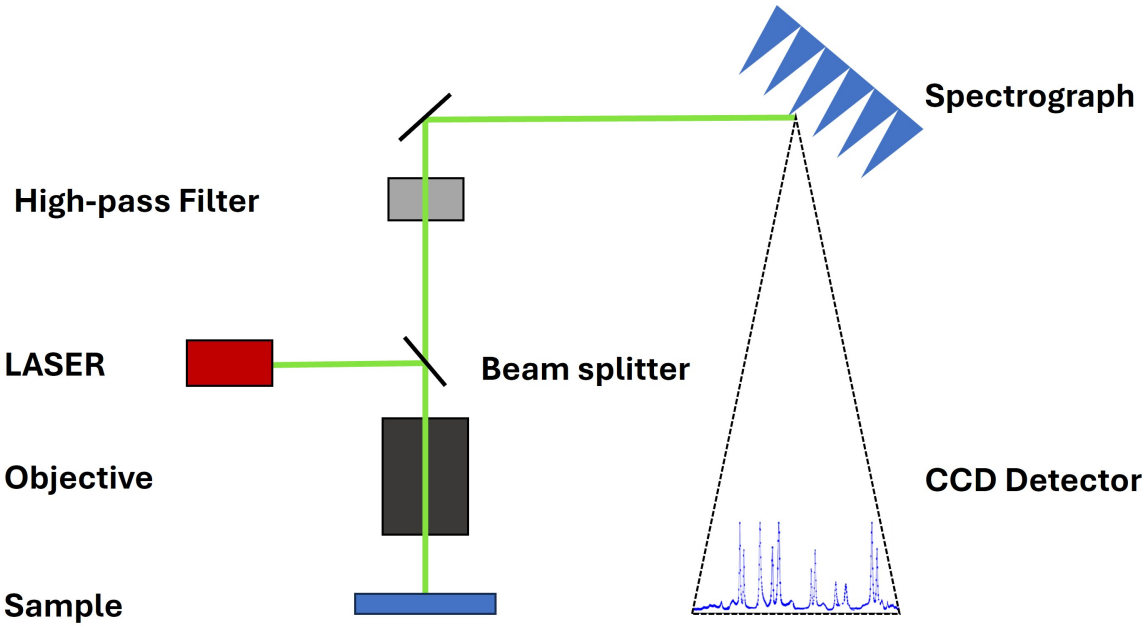

Figure 6: Schematic of a Raman setup

Chapter 2

Methods

This project uses patterns etched into SiO_2 to stress our MoS_2. A photomask was designed and manufactured to replicate those patterns into our substrates. We then exfoliated, identified, and transferred different layers of MoS_2 on top of the patterns before characterizing the strained nature of the samples via Raman spectroscopy. The first step of that process is to fabricate our patterned structures is to etch the features.

2.1 Photolithography

Photolithography was chosen to fabricate the patterned substrates. This process relies on a photomask, a plate that allows UV light to pass through in certain areas, to then expose a photosensitive polymer spun on a wafer. This leads to a change in the polymer solubility and thus allows the use of a developer to strip it where it was exposed (in the case of a positive photoresist). This defines the desired patterns in the photoresist which we can replicate in our Si-SiO_2 substrates using an etching process, explained in section 2.2. The design of our photomask for the purpose of this project is explained below, with a more in-depth explanation in Appendix A.

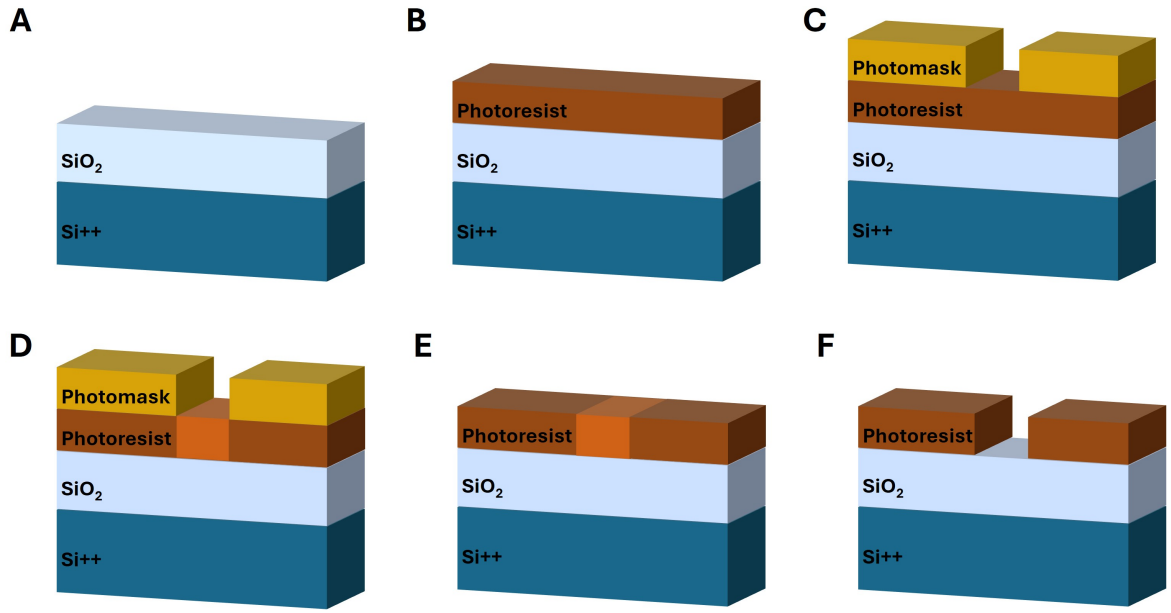

Figure 7: Six-step process for exposure and development of the patterns. A) Substrate cleaning. B) Photoresist spinning. C) Photomask alignment. D) Exposure. E) Post-exposure bake. F) Development.

2.1.1 Design of the photomask

The geometries we designed are shown in Figure 8 A-D. We designed them using a GDS editor, which is binary file format used to encode planar geometries. The initial goal was to design four types of geometries to test if they led to different forms of strained MoS_2. The photomask is shown in Figure 8. The geometries are a set of 1D trenches (A), a square array of circular dots (B), a triangular array of circular dots (C) and a square array of triangles (D). We also varied the geometry parameters: we varied the feature size as well as the spacing. These other geometries were explored but not used due to the limited resolution of photolithography leading in most of our tests to poor feature fidelity. More details about the GDS file as well as the other patterns with limited resolution are shown in Appendix A.

Photolithography has a minimum resolution of ≈ 1 μm. Trying to manufacture a mask with features under that threshold leads to infidelities. It can be seen in Figure 8 E-H

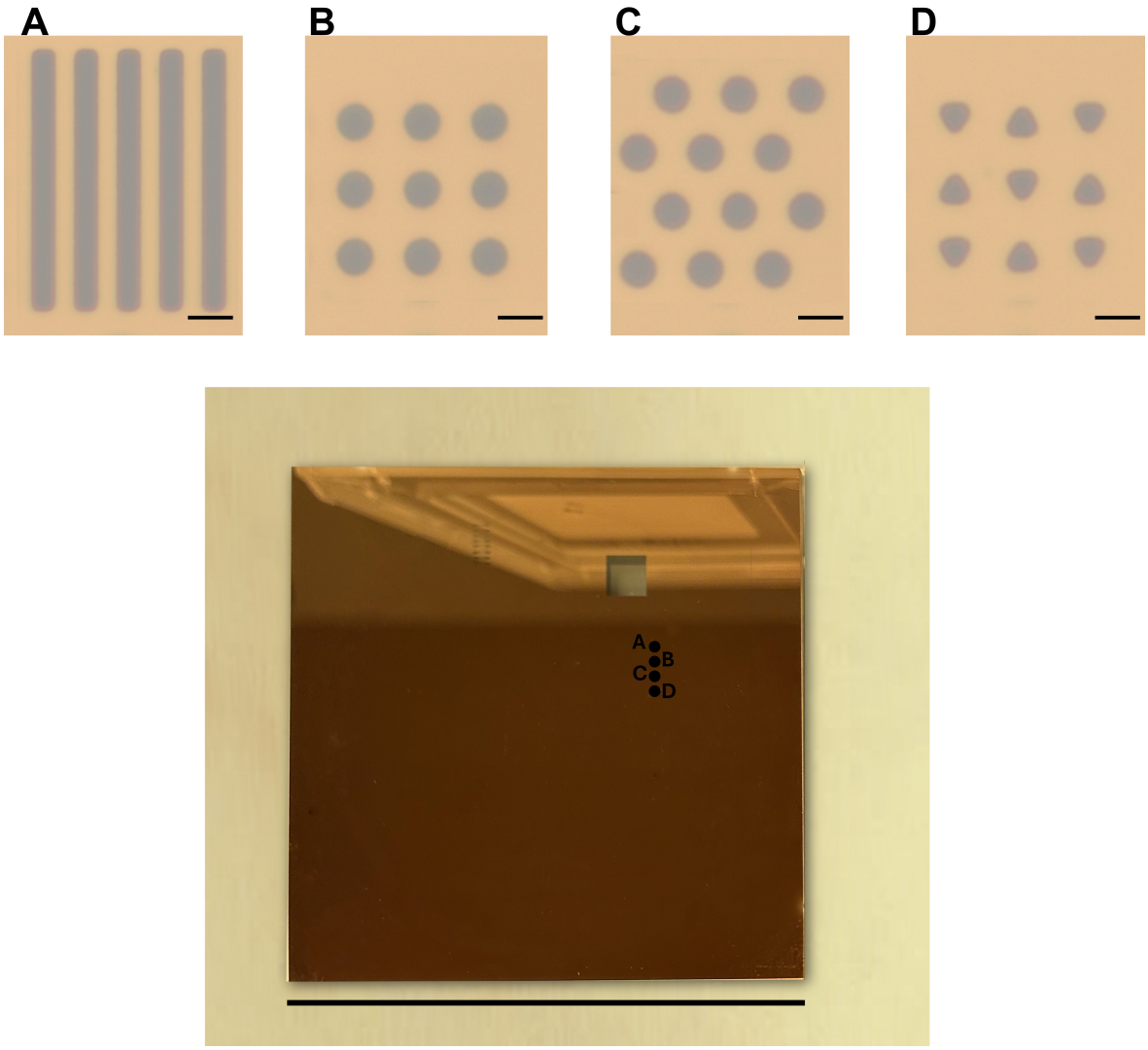

Figure 8: The four types of pattern geometries explored.
A) - D) show a set of 1D trenches, a square array of circular dots, a triangular array of circular dots and a square array of triangles respectively as they appear on the photomask. The scale bars represent 5 μm. These specific patterns correspond to a spacing of 5 μm and a feature length of 2 μm. Their position is shown on the photomask, displayed below. The square opening on the mask is used to guarantee adhesion between the mask and the photoresist, more details are provided in Appendix A. The scale bar on the photomask is 10.16 cm

that the photomask itself was affected by the broadening (rounder edges seen in E and H, larger feature sizes). The equation that determines the linewidth is [86]:

$$l \approx \sqrt{\lambda(g + \frac{d}{2})} \tag{2.1}$$

Where λ is the exposing radiation wavelength, g the gap between the mask and the photoresist, and d the photoresist thickness. Assuming a wavelength of 365 nm, a gap of 5 μm and a photoresist thickness of 750 nm, we obtain a minimum resolvable linewidth of 1.4 μm. Our different trials had a high failure rate for features close to this limit, which is why we chose to concentrate our effort on the largest features we could reliably obtain.

2.1.2 Exposure and development

Figure 7 illustrates the evolution of the wafers through the exposure and development steps.

Step A: Surface preparation. The goal of this step is to remove potential contamination on the wafers, which negatively impacts the quality of substrates. We cleaned our wafers by dipping them in subsequent baths of Acetone, Isopropanol (IPA) and Deizonized (DI) water for up to 5 min, before blowing off the remaining water droplets with N_2. We also removed any water residuals that could remain by dehydrating the wafers on a hot plate.

Step B: Photoresist film deposition. The choice of photoresist is essential to ensure high fidelity and resolution. To distribute it evenly on our wafers, we used a spin-coater (Laurell WS-650-23) to dispense our photoresist SPR955 at 6000rpm. Baking our wafers for 5 min at 90 C immediately after the spinning is crucial to ensure that the solvents are evaporated and also improves uniformity. This process leads to a thickness of 750nm of SPR955 [87].

Step C: Mask alignment. The substrate is then placed into a mask aligner (Near-UV OAI 204IR), before loading our photomask while ensuring proper x and y alignment of the mask to ensure good feature fidelity. Maximizing contact between the wafers and the photomask (z alignment) is also crucial to avoid broadening of the features, although not completely avoidable.

Step D: Exposure. Ultraviolet light is used to expose the photoresist in the desired areas. The reaction threshold energy dosage for SPR-955 is 95 mJ/cm^2 while the light intensity was measured to be 9.00 mW/cm^2. The exposure time was therefore calculated to be 10.5 s.

Step E: Post-exposure bake. Baking our wafers at 120 for 5 min after the exposure ensures that the photoresist stops reacting with ambient light smoothing of the surface.

Step F: Development. Developing our wafers by leaving them in a continuously-swirled bath of MF-24 for 1 min leads to well-defined photoresist edges. Transferring our wafers into a bath of DI water stops the development process.

These steps are crucial and must be done with extreme attention to limit the creation of unwanted features or broadenings. Development plays an especially important role, as leaving the features to develop for too short leads to incomplete and shallow etches while leaving them to develop for too long leads to strong broadening or even complete losses of the features. There will always be variations between the desired features and the obtained ones. We show in Figure 25 an example of a pattern which was lithographed correctly onto the photomask (notwithstanding a slight broadening) but incorrectly during our lithography attempts. This issue most likely comes from a combination of an exposure broadening and a slightly too long development.

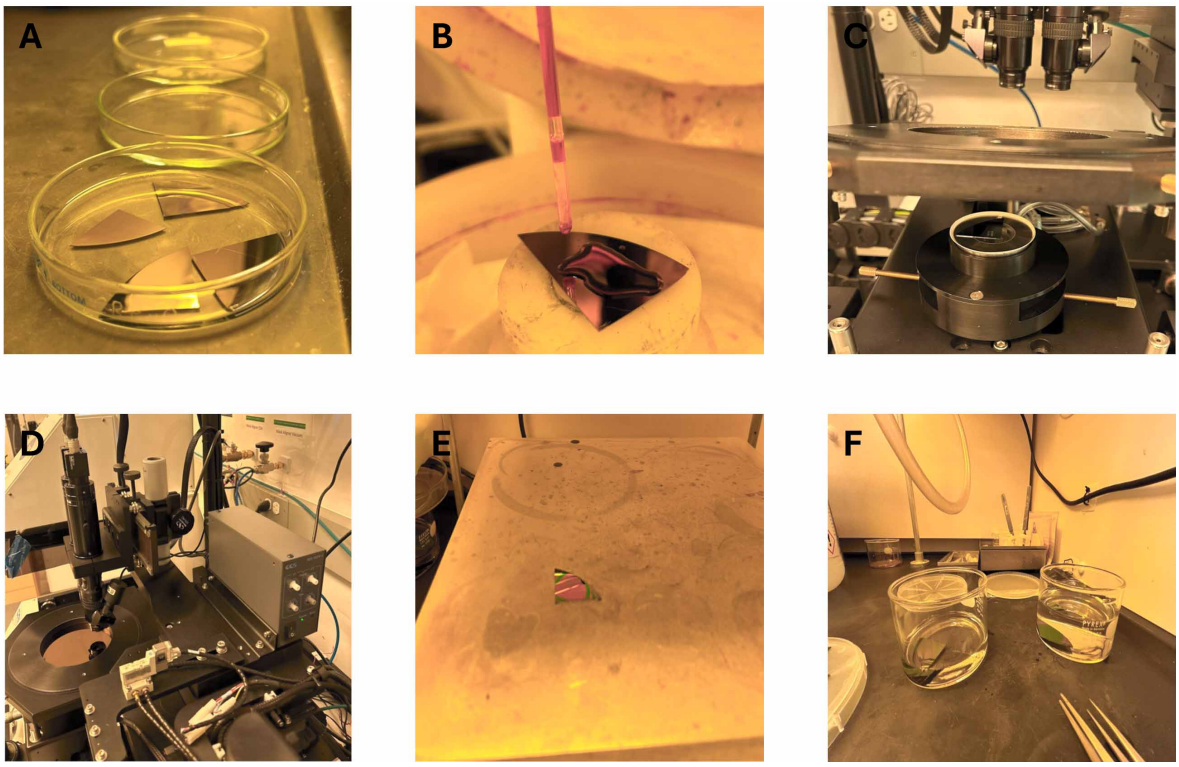

Figure 9: Images taken during steps A) - F).
A) Substrate cleaning in Acetone, IPA and DI water. B) Dispensation of photoresist on the substrate in the spinner. C) Substrate loading in the mask aligner. D) Camera-aided alignment of photomask and substrate. E) Post-exposure bake. F) Development.

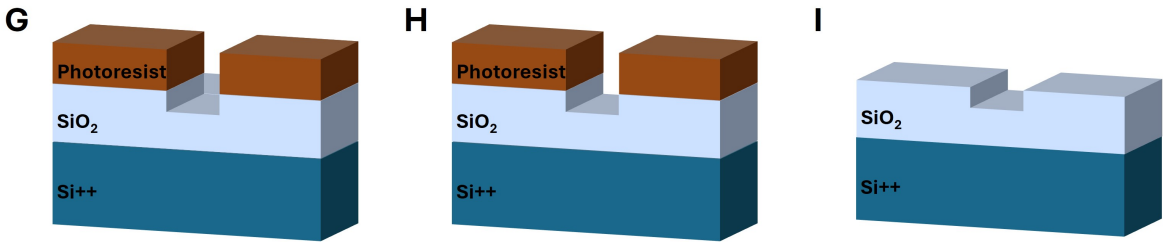

Figure 10: 3-step process to etch the patterns into the substrate.
G) RIE etching. H) Photoresist removal. I) Cleaning.

2.2 Creating patterns by reactive ion etching (RIE)

Once the desired patterns are developed into our polymer, an etching process is run to replicate the periodic patterns into our substrate. We opted for reactive ion etching (RIE), a dry etching method in which a plasma accelerates electrons and ions onto a material, leading to a controlled destruction. Dry etching is anisotropic, meaning that the vertical etching rate is much higher than the sidewall etching rate: this leads to a higher fidelity between the developed and the etched patterns. The polymer will also be etched by the process, which is why it is important to prioritize the selectivity of a given process recipe. Ours was developed by starting with etchants known to have high SiO_2 selectivity - Ar and Tetrafluoromethane (CF_4) and improved by performing etching tests. To establish the etch rate value, we followed the same process with varying time to see the evolution of the SiO_2 thickness. The final recipe we used uses 25 sccm of CF_4 & 10 sccm Ar at 100 W and 8 Pa in our SAMCO RIE-10NR system, for an expected SiO_2 etch rate of 25 nm/min. Our substrates are made of 285nm of thermal SiO_2 oxide on doped Si (represented by SI++ on the Figures).

Step G: RIE etching. By loading our wafers into our RIE system and processing them as mentioned above for 30s, we expect an etch of 12.5 nm.

Step H: Photoresist removal. By first submerging our wafers in Remover 1165 for 5 min at 60°C, then in a different bath at room temperature overnight, we eliminate most of

the leftover photoresist.

Step I: Cleaning. By running ultrasonic cleaning processes in Acetone, IPA and DI water at 80kHz and 37kHz, we further ensure the cleanliness of our substrates.

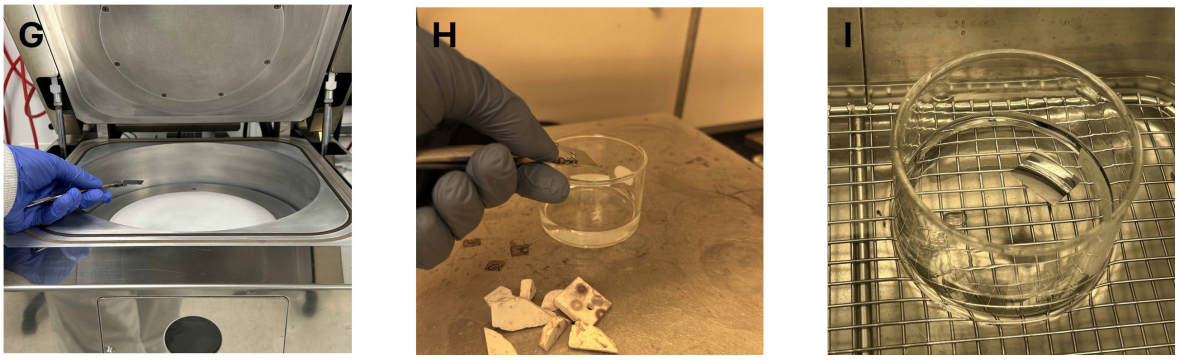

Figure 11: Images taken during steps G) - I).
G) Loading of the substrates in the RIE system. H) Photoresist removal. I) Ultrasonic processes cleaning.

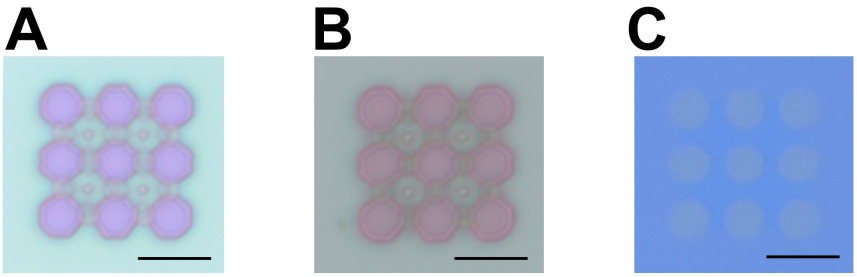

Figure 12: Optical evolution of a pattern at different stages of the photolithographic process.
A) After development. B) After etching. C) After cleaning the photoresist. The scale bars represent 5 μm.

Figure 12 shows the evolution of a set of patterns at different steps: Figure 12 A) shows an example of a developed pattern, corresponding to step F). We immediately notice slight exposure of other unwanted features between the desired patterns, which persist

after the etching process, shown in Figure 12 B), corresponding to step G) of RIE. Figure 12 C) shows the resulting features after cleaning the photoresist, representing step I). We notice immediately that not all the features present in Figure 12 B) led to an etched feature in Figure 12 C). This signifies that in those areas, the etching process did not etch enough to reach and etch the substrate. This can be explained by the partial exposure of the photoresist, leading to a lower solubility of the resist in these regions.

2.3 Transfer of MoS_2 on periodic patterns

The final step in the fabrication of our patterned structures is to assemble them via transferring the 2D material flakes onto our Si/SiO_2 substrates. The first step of the transfer is the exfoliation of the material using tape: the standard technique consists of adding a small amount of crystal onto a $\approx$ 5x5 cm^2 tape square before repeatedly folding it onto itself, thinning down the crystal enough to lead to large ($> 50\ \mu m^2$) thin flakes. Appendix B shows the steps to obtain thin flakes, a picture of exfoliated MoS_2, as well as our transfer setup.

After the exfoliation of MoS_2, a square of Polydimethylsiloxane (PDMS) - a deformable, inexpensive and robust material - is then pressed onto the flakes to pick them up, as shown in Figure 13 A). After carefully peeling off the PDMS as to cause the least amount of tearing, it is affixed on a glass slide to allow for optical microscope inspection and identification of the desired MoS_2 flakes (Figure 13 B)). The temperature of the stage is set to 80 °C to facilitate the drop-off [88], which is done by progressively lowering the glass slide onto our substrate while ensuring proper alignment of the flakes with the patterned substrates (Figure 13 C)). Maintaining contact for more than 1 minute before slowly separating the stages leads to the MoS_2 flake being dropped off onto the patterned substrate (Figure 13 D).

Many attempts were made to identify thin (aiming for single-layer) flakes and drop

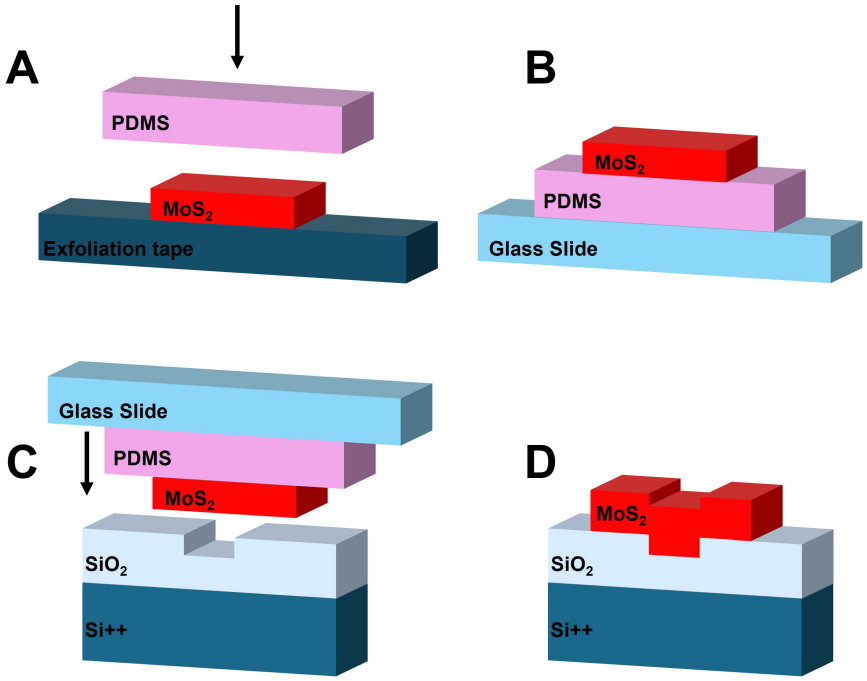

Figure 13: Assembly procedure to transfer MoS_2 thin layers onto patterned substrates. A) The MoS_2 is exfoliated onto tape and PDMS is pressed down on the flakes. B) The PDMS is flipped and affixed onto a glass slide. C) The stack is dropped off onto the patterned areas. D) Finished structure.

them off on top of the patterns, and around 10 % of the flakes we picked up were successfully dropped off in the right location, as the weak adhesion of the PDMS to the substrate led to a noticeable (< 20 μm) shift between the initial and the final drop off location. On top of this, the stronger adhesion between the PDMS and the MoS_2 than between the MoS_2 and the substrate led to some transfers requiring multiple attempts or only working for a much faster release of the stage.

We focused our study on one of these successful transfers, which is shown in Figures 14 B) and D). Figure 15 highlights in yellow areas of the MoS_2 that were initially dropped off, but ultimately detached themselves. It is not clear to us what caused this separation, although the fragilization of the flake due to the repeated drop-off attempts of this specific flake could explain this phenomenon.

Figure 16 shows optical and atomic force microscope (AFM) images of MoS_2 flakes

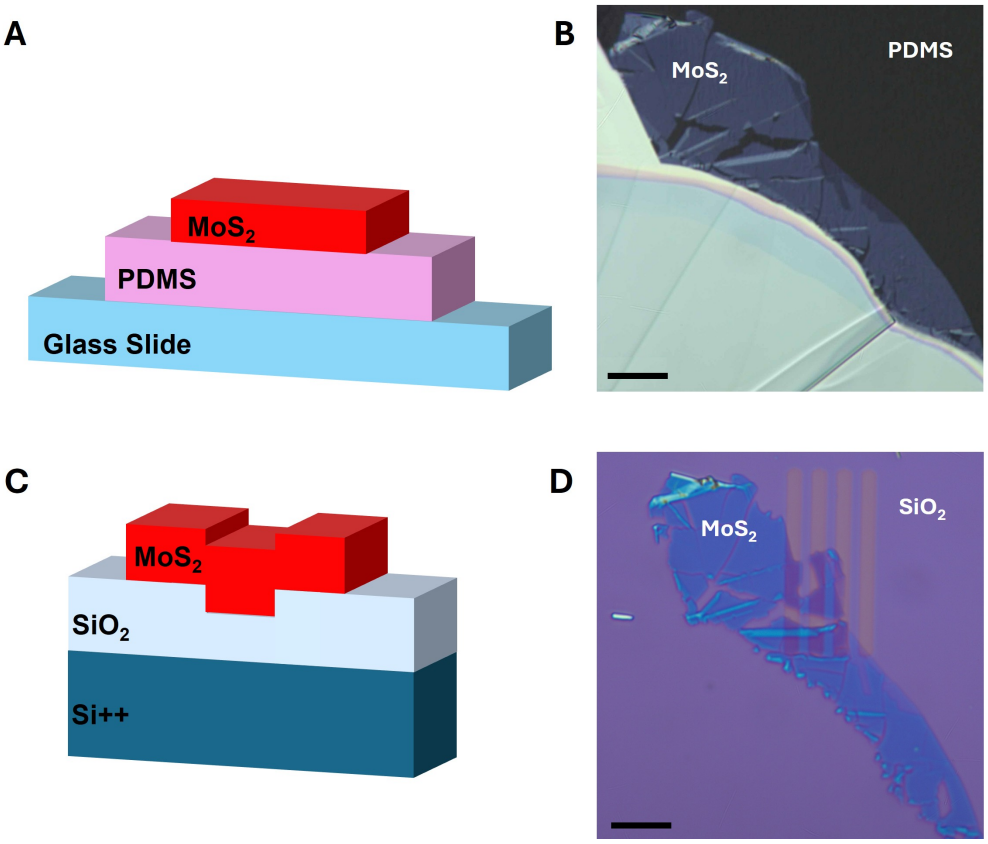

Figure 14: Optical images of the MoS_2 flake before and after the transfer. A) Schematics from Figure 13 B). B) Optical image of the MoS_2 on the PDMS stamp (image was flipped vertically for clarity), matching the schematics in A). C) Schematics from Figure 13 D). D) Optical image of the flake once transferred on top of a 1D trenches patterns, matching the schematics in C). The scale bars represent 10 μm.

which were dropped off on top of the MoS_2 patterns. Some transfers suffered from too intense lateral shifts during drop offs, leading to a drop-off location being too far off from the patterns, like in D). In other cases, the drop off was incomplete and only part of the flakes were dropped off, like in Figure 16 A) and G). These drop-offs were done on different geometries, like 1D trenches, shown in C) and L), square arrays of dots, as shown in F), and square arrays of triangles - as seen in I) - although the loss of features makes it hard to distinguish these triangles from dots.

The more standard approach of picking up and dropping off few-layers of 2D materials

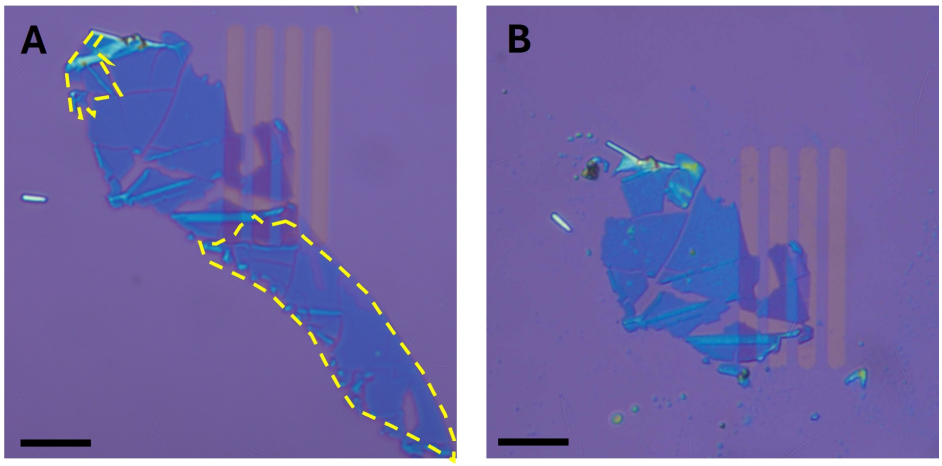

Figure 15: Optical image of the flake
A) Initial dropped flake. B) Dropped flake after involuntary breaking. The scale bars represent 10 μm.

involves using a glass slide with Polypropylene carbonate (PPC) spun on it to first pick up and then drop off the desired flakes, before melting the PPC off. This technique does not allow for precise control of the location of the dropoff. Another problem lies in the melting of the polymer, which we were concerned could completely quench our patterns and interfere with the topographic and Raman spectroscopy maps. To increase the cleanliness of our flakes, they were subjected to a thermal annealing process after the transfer.

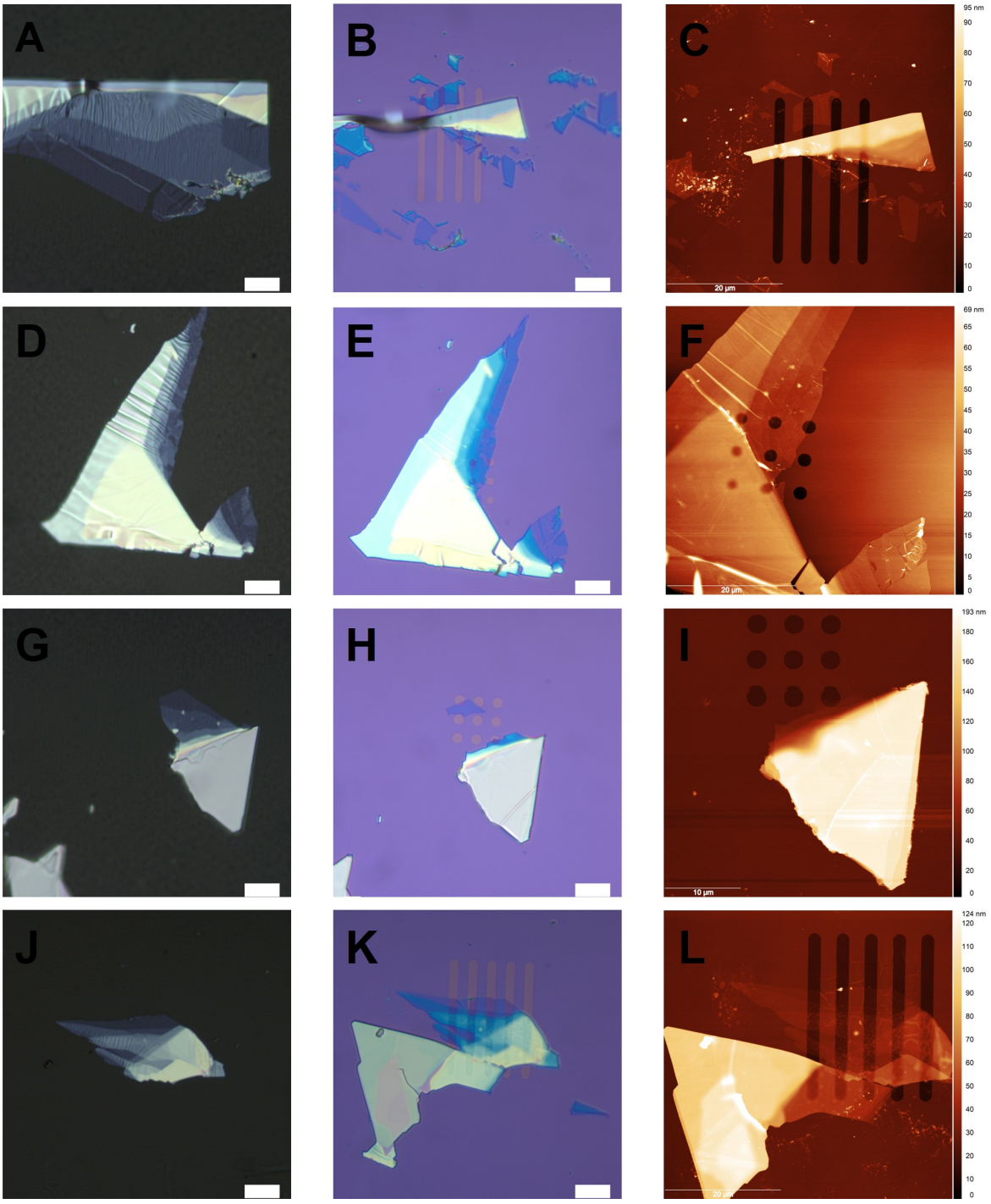

Figure 16: Optical images of MoS_2 flakes on the PDMS square (A), D), G), J)), once transferred (B), E), H), K)), and corresponding AFM scans (C), F), I), L)). The scale bars on the optical images represent 10μm.

Chapter 3

Results and discussion

AFM scans of the MoS_2 flake transferred on a patterned substrate were conducted to obtain topographic data and are shown in Figures 17 A) and B). Tears and large ($>$ μm^2) bubbles can be seen, the presence of which can be exacerbated by the suddenness of the MoS_2 drop-off which causes air bubbles to be trapped. As mentioned previously, a section of the MoS_2 was ripped apart, and a section of the flake folded onto itself, which can be seen in the bottom right of 17 B). Figure 17 C) and D) show that according to our AFM scans, the flake lies on trenches of width 2.3 μm and of depth 13.2 nm, while the expected width is 2 μm and the expected depth is 12.5 nm. These discrepancies can be explained by photolithography broadening phenomena explained in Section 2.1.1 and etching effects explained in Section 2.2. The green profile shown in 17 E) shows the step edge from substrate to thin flake (from first to second plateau), as well as the step edge from substrate to the thicker area flake (from first to third plateau). The thicknesses of these flakes are 3.2 $\pm$ 0.5 nm and 6.0 $\pm$ 0.5 nm, which correspond respectively to approximately 4 and 8 layers (MoS_2 layer thickness $\approx$ 0.75 nm). One of the main factor of these uncertainties comes from the extreme amount of air bubbles under the MoS_2 which artificially increase the height of the profiles. Repeating the line profile inside one of the trenches (purple profile in 17 E)) shows thicknesses of 2.8 $\pm$

0.4 nm and 5.4 ± 0.5 nm. These values are still within the error margin of one another, but it is possible that the reduced step height of the flake inside the trench comes from enhanced conformity of MoS_2 within the pattern due to the progressive lowering of the flake onto the area during drop off.

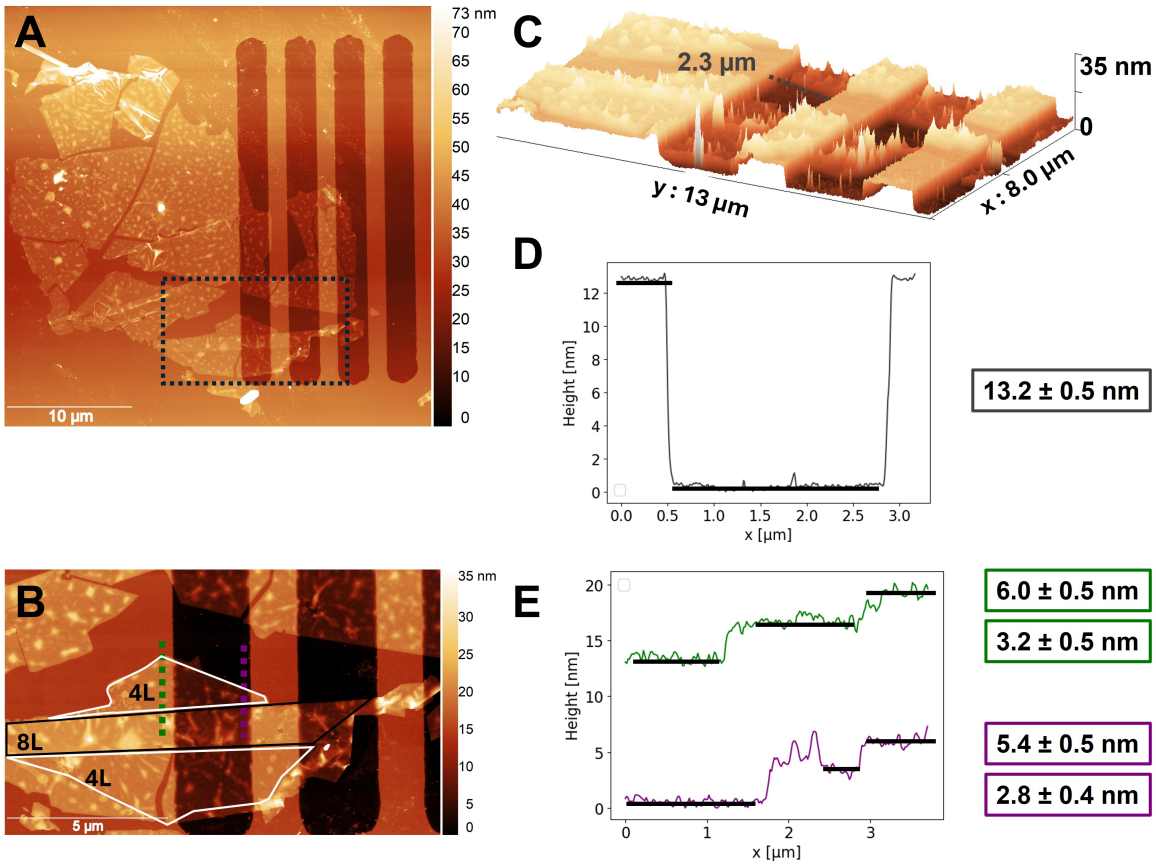

Figure 17: AFM of MoS_2.

A) Scan of the entire flake. B) Zoom of AFM scan focused on the region highlighted in dashed lines in A). Black and white-outlined areas correspond to 8-layer and 4-layer thick regions. C) 3D map of B). D) Line profile along dashed line in C). E) Line profiles along the dashed lines in B). Scans were done at 1024 scans/line and 0.3 Hz on a Bruker AFM in tapping mode

As mentioned before, Raman spectroscopy can be used to characterize the number of layers in crystalline systems: Figure 18 A) shows the AFM overlaid with how the individual scans were rastered: the beam (of spot size 0.5 μm) scans horizontally first and vertically second with a spacing of 0.35 μm, from the bottom right to the top left. The spacing was chosen on purpose smaller than the beam spot size as it offers a good compromise between a complete sampling of the area and scan time. The coloured circles represent the position corresponding to the Raman scans in Figure 18 B). The brown circle corresponds to a scan taken in the 8-layer region, while the purple one corresponds to a scan from the 4-layer region. We observe a shift of the peak positions between the two: the purple curve shows peaks at 384.1 cm^{-1} and 405.6 cm^{-1}, while the brown curve (corresponding to the 8-layer region) shows peaks at 383.2 cm^{-1} and 407 cm^{-1}. While we do observe a shift of the modes, we want to have a more rigorous approach by averaging values over an entire region.

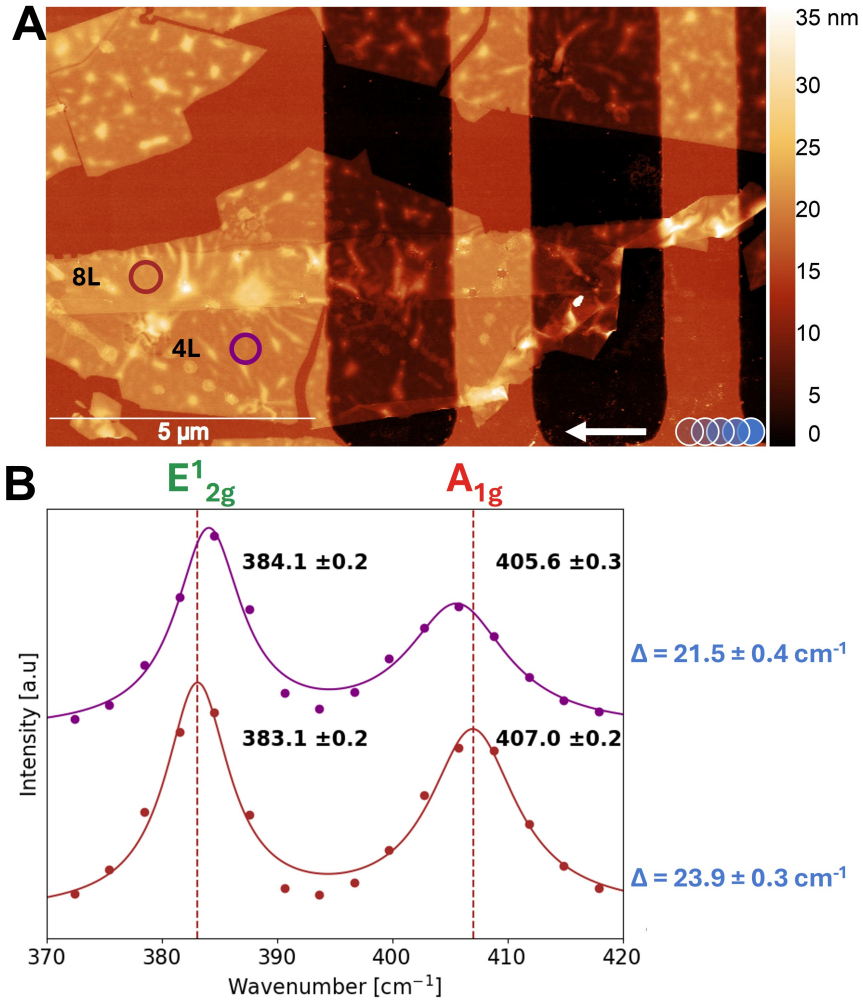

Figure 18: Difference in Raman response for different thicknesses. A) AFM scan with an overlay of the raster parameters. B) Raman spectra taken at the corresponding points shown in A). The fitted peak position of the modes are shown as well as their difference (in blue).

Raman artifacts, noise and local effects (like tears, bubbles, doping) present in individual spectra can obscure our analysis, and to limit these effects, we investigated how the response varies across the flake: maps of the peak positions are shown in Figure 19. A), B) and C) show maps of the evolution of the E^1_{2g}, A_{1g} and A_{1g} - E^1_{2g} peak positions across the flake respectively, while D) shows the AFM scan. The maps and the AFM

scan feature the coloured squares shown in Figure 18 A) as circles.

The regions corresponding to the 4 and 8-layer regions are outlined in black and white respectively on Figure 19 C) and D). By averaging the values in each area, we obtain an average in the 4-layer region (black outline) for the E^1_{2g}, A_{1g} and A_{1g} - E^1_{2g} modes of 384.2 $\pm$ 0.5 cm^{-1}, 405.7 $\pm$ 0.5 cm^{-1} and 21.6 $\pm$ 0.2 cm^{-1}. For the 8-layer region (white outline), these values are 383.7 $\pm$ 1.0 cm^{-1}, 407.2 $\pm$ 0.7 cm^{-1}, and 23.5 $\pm$ 0.5 cm^{-1}. This increase of the separation of the peaks for increasing thickness has been widely observed in other studies (as mentioned in Section 1.3.3), although other studies with the same laser excitation on exfoliated MoS_2 have found that the specific values we obtained correspond to thinner MoS_2 [72, 73, 89, 90]. This discrepancy can most likely be attributed to the omnipresence of air bubbles, which can both increase the step heights obtained via AFM scans, as well as disturb the vibrational modes of the material. We used the Horiba Xplora Plus to take our Raman measurements with a LASER at 532nm (corresponding to an energy of 0.37eV), and we used the widely available python library lmfit [91, 92] to fit lorentzians to our Raman datasets, from which we obtained the fitted peak positions, as well as the standard error of those peak positions. Appendix C shows a version of the code we employed to fit our datasets, extract the peak positions and produce Raman spatial maps.

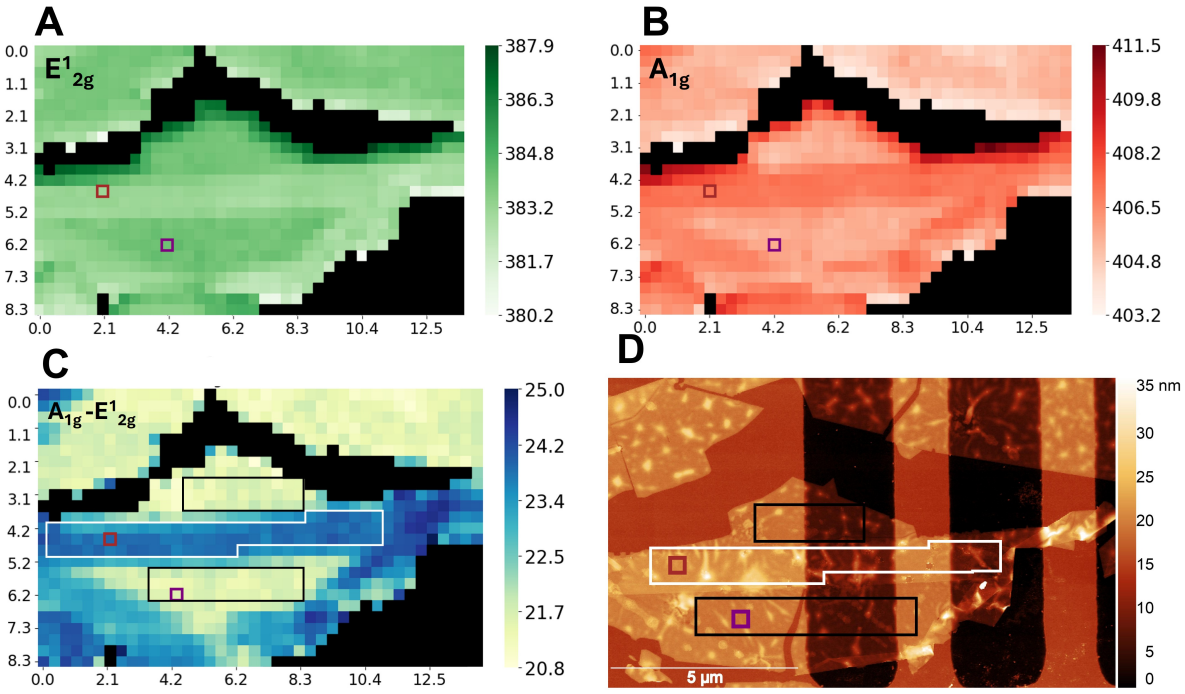

Figure 19: Maps of Raman shifts modes of MoS_2 on patterned substrate. A) Map of the E^1_{2g} peak position. B) Map of the A_{1g} peak position. C) Map of the difference of the two modes. The color bars represent the Raman shift in cm^{-1}. D) AFM scan overlaid with the two regions.

Figure 20 A) shows the AFM scan where two large bubbles are highlighted by black dotted rectangles. Figures B) shows a 3D view of these regions, while Figure C) shows the map of the $A_{1g} - E^1_{2g}$ peak position, where two areas corresponding to the bubbles in A) and B) are marked by similar black dotted rectangles. Figure 20 D) shows the column-averaged response of $A_{1g} - E^1_{2g}$ at five successive x positions, corresponding to the data outlined. Our data suggests a slight softening of $A_{1g} - E^1_{2g}$ due to the presence of a bubble. This contradicts typical findings about the effect of bubbles on the Raman response of MoS_2, where the applied biaxial tensile strain causes a much greater red-shift of the E^1_{2g} mode than the A_{1g} mode [43], resulting in a hareding of $A_{1g} - E^1_{2g}$. Commenting further about the nature of the strain caused by the bubbles

proves challenging as the order of magnitude of the spectral uncertainty is greater than the change in Raman response.

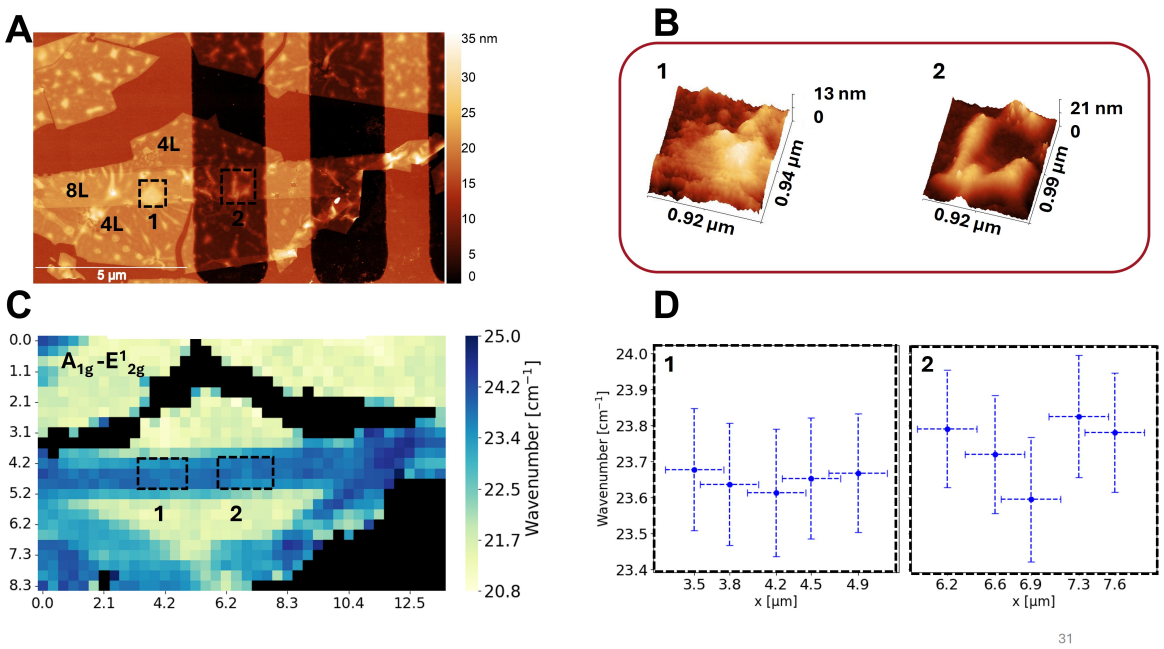

Figure 20: Raman response of MoS_2 due to trapped air bubbles.
A) AFM scan. B) 3D view of selected regions from A). C) Raman map of $A_{1g} - E^1_{2g}$ peak positions. D) Column-averaged response of $A_{1g} - E^1_{2g}$ along the x-axis in C), with each point averaged over 3 same-column values.

The x-uncertainty in 20 D) relates to the spatial uncertainty, which is linked to the beam spot size of 0.5 μm. Thermal broadenings, optical settings and surface response can all influence the beam size. A larger beam spot size samples a larger area for each pixel of the map, which averages the values and limits the resolution. To illustrate the influence of beam spot size on our data, we are showing in Figure 21 C) the comparison between 3 plots, one taken within a homogeneous MoS_2 area (in purple), another from a pixel bordering exposed SiO_2 (in grey) and the third one from exposed SiO_2 (in yellow). These pixels are all shown by circle of the same color outline in A) and B).

The response of the exposed SiO_2 shows a non-significant variation of the intensity. The pixel bordering the exposed SiO_2 shows the known peaks of the MoS_2, although the influence of the neighbouring SiO_2 can be seen by a general loss of quality and a broadening of the peaks. That influence is weaker in the response from the pixel in the middle of the MoS_2. Comparing the purple and the grey plot in C) shows that each pixel samples data from a larger area around the pixel.

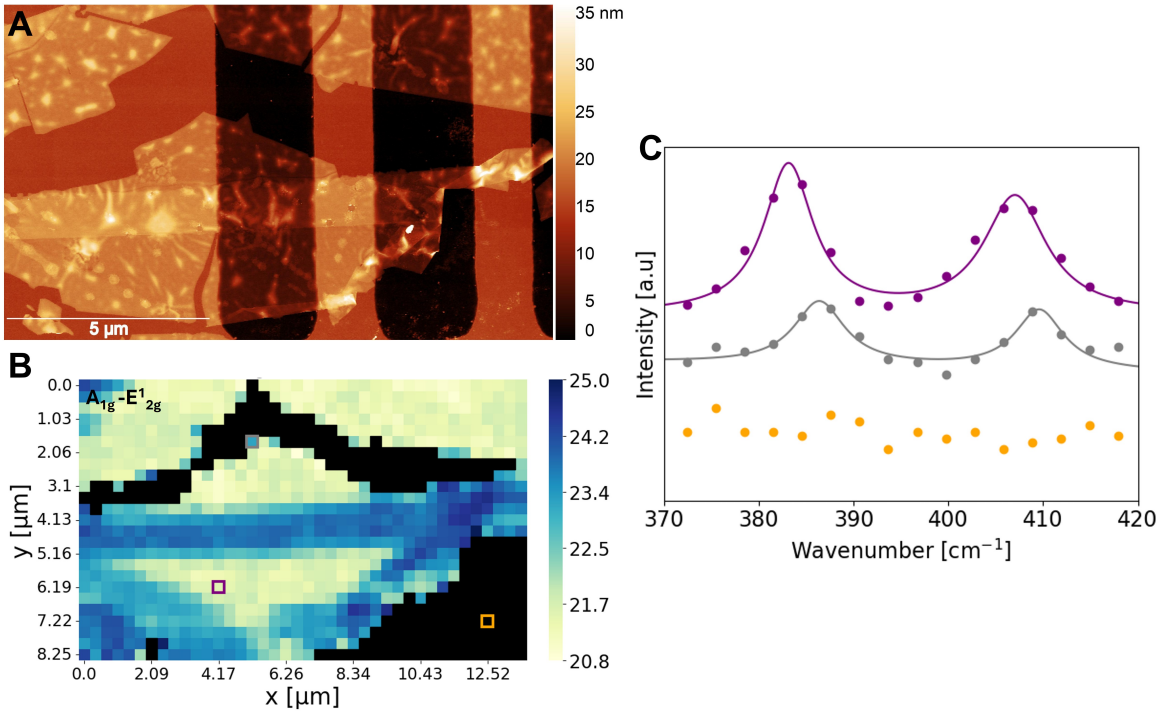

Figure 21: Line profiles at 3 different positions.
A) AFM scan. B) Raman map of the $A_{1g} - E^1_{2g}$ evolution. C) Raman datasets at 3 different locations.

Another contributor to the spatial uncertainty of the maps is the drifting of the system. Over the course of the scans, thermal, optical and mechanical instabilities influence the system and cause a gradual drifting of the system. By comparing the optics before and after the scans, we quantified the system to have drifted by 0.83 μm in the x-

direction and by -1.24 μm in the y-direction over the duration of the scan. The data was collected in a raster configuration, from right to left and from bottom to right, which means the drift effects are most severe in the top left corner. This explains for instance the response in the top-left corner of our maps, which corresponds in reality to out-of-frame thicker MoS_2 that can be seen left of the top of the dotted outline in the AFM of Figure 17 A). This also explains the discrepancy in the width of the exposed SiO_2 channel compared to optical and topographical data. This effect directly affects our ability to observe shifts due to bubbles, or even trenches.

The y-uncertainty in Figure 20 D) corresponds to the standard error of our fitted peak positions. Raman system gratings also have a spectral resolution, which denotes its capacity to detect two peaks being separate. This is not a problem in our study since the two peaks are far apart. The spectral step size (as in, the spectral spacing between two points) can be reduced by choosing a grating with a higher resolution. This comes at the cost of response intensity and acquisition speed, which is crucial to minimize due to potential overexposure and the aforementioned drift.

By instead monitoring the response near the edge of a pattern (Figure 22 D)), we observe a slight shift of the $A_{1g} - E^1_{2g}$ peak position, although that change is not significant enough for us to comment on with certainty.

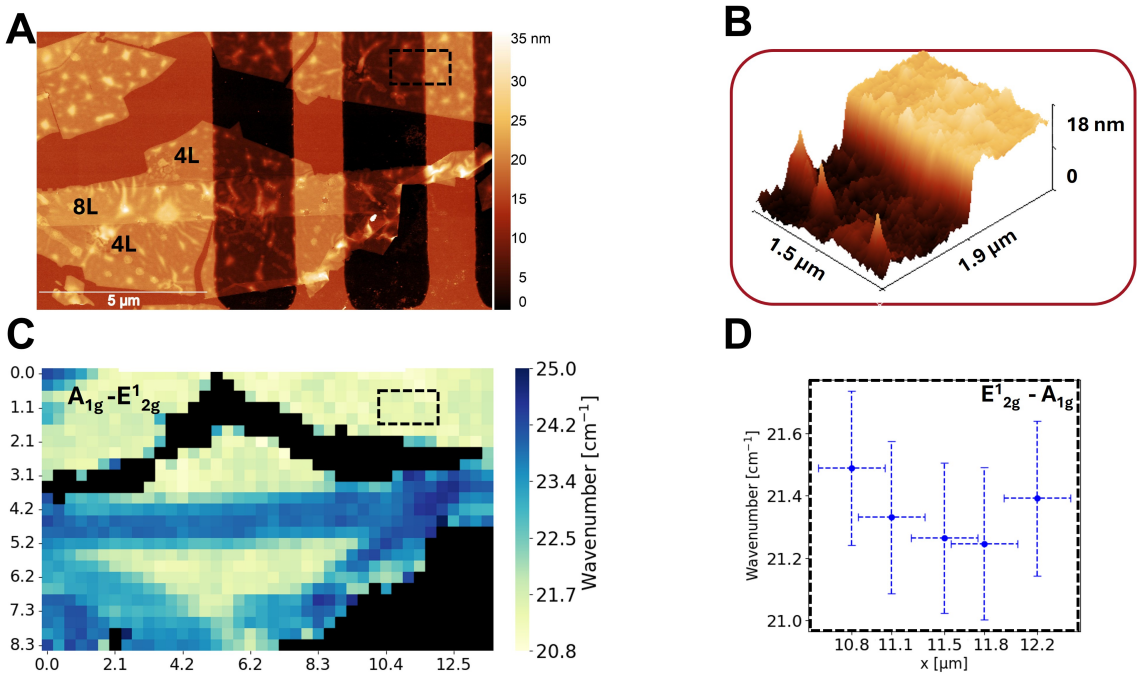

Figure 22: Raman response of MoS_2 due to patterned substrate.
A) AFM scan. B) 3D view of selected regions from A). C) Raman map of $A_{1g} - E^1_{2g}$ peak positions. D) Column-averaged response of $A_{1g} - E^1_{2g}$ along the x-axis in C), with each point averaged over 3 same-column values.

The height of the features is the limiting factors of this study: other studies using similar methods have heights of an order of magnitude higher [41, 45, 46, 67, 68], which are responsible for more pronounced strain gradients and measurable Raman shifts, suggesting that our current geometry induces strain that cannot be resolved with our Raman system. Raman studies of strain engineering are able to use shift rates previously obtained from geometries that can induce tunable strains to estimate the percentage of strain of their own samples. Under biaxial strain for instance, the E^1_{2g} mode sees a redshift of 5.2 cm^{-1} per % of strain [65,93]. With our spectral step size of 2.96cm^{-1}, the minimum amount of strain we could have resolved is 0.57%. The inability to observe a significant change in the Raman shift response prevents us from quantifying the amount

of strain our system experiences. Future work, with deeper features to induce stronger strain, could also explore the different pattern geometries we mentioned (1D trenches, circle and triangular array of holes as well as circle arrays of triangles) to observe if and how the Raman response is affected by the geometries.

Chapter 4

Conclusion and Outlook

In conclusion, this study investigated the topography and strain characteristics of MoS_2 flakes transferred onto a periodically patterned substrate using AFM and Raman spectroscopy. The AFM scans revealed clear morphological features such as tears, folds, and trapped air bubbles, resulting from the drop-off method. The measured trench dimensions slightly deviate from the theoretical values due to broadening effects and etching variability. Raman spectroscopy confirmed the presence of regions with different layer thicknesses, as evidenced by the peak position and separation of the E^1_{2g} and A_{1g} modes. The observed spectral shifts in the 4-layer and 8-layer regions differ quantitatively from previously reported values, which might result from an misestimation of the flake height due to interfacial bubbles, as well as a change in the Raman response due to the omnipresence of these bubbles and effects resulting from the broadening of the beam spot size. While our data suggests slight strain modulations of the Raman response on the patterns, at their edges, or near the bubbles, the magnitudes of these shifts fall well within the uncertainty range of our measurements. This lack of pronounced spectral shift can be attributed to the shallow depth of the patterns, which induces strain we cannot resolve with our Raman system. Other limitations like beam spot size broadening and noticeable drift further complexify this study with our current setup. Future

studies employing higher-resolution Raman systems or deeper substrates features may be necessary to more definitely characterize strain distributions in transferred MoS_2 flakes. Substrate engineering provides a way to realize scalable, reconfigurable platforms for quantum and optoelectronic applications based on MoS_2 and related TMDs as explored in [94–100]

List of Figures

Bibliography

[1] Novoselov, K. S. *et al.* Electric field effect in atomically thin carbon films. *Science* **306**, 666–669 (2004).

[2] Ajayan, P., Kim, P. & Banerjee, K. Two-dimensional van der waals materials. *Physics Today* **69**, 38–44 (2016).

[3] Manzeli, S., Ovchinnikov, D., Pasquier, D., Yazyev, O. V. & Kis, A. 2d transition metal dichalcogenides. *Nature Reviews Materials* **2**, 17033 (2017).

[4] Cho, B. & Kim, Y. Preparation and properties of 2d materials. *Nanomaterials* **10** (2020).

[5] Montblanch, A. R.-P., Barbone, M., Aharonovich, I., Atatüre, M. & Ferrari, A. C. Layered materials as a platform for quantum technologies. *Nature Nanotechnology* **18**, 555–571 (2023).

[6] Duan, X. & Zhang, H. Introduction: Two-dimensional layered transition metal dichalcogenides. *Chemical Reviews* **124**, 10619–10622 (2024).

[7] Akinwande, D. *et al.* A review on mechanics and mechanical properties of 2d materials—graphene and beyond. *Extreme Mechanics Letters* **13**, 42–77 (2017).

[8] Papageorgiou, D. G., Dong, M., Zhang, H., Liu, M. & Young, R. J. Mechanical properties of transition metal dichalcogenides: towards high-performance polymer nanocomposites. *2D Materials* **12**, 012002 (2024).

[9] Kazemi, S. A., Yengejeh, S. I., Wang, V., Wen, W. & Wang, Y. Theoretical understanding of electronic and mechanical properties of 1t transition metal dichalcogenide crystals. *Beilstein Journal of Nanotechnology* **13**, 160–171 (2022).

[10] Liu, K. & Wu, J. Mechanical properties of two-dimensional materials and heterostructures. *Journal of Materials Research* **31**, 832–844 (2016).

[11] Wang, Q. H., Kalantar-Zadeh, K., Kis, A., Coleman, J. N. & Strano, M. S. Electronics and optoelectronics of two-dimensional transition metal dichalcogenides. *Nature Nanotechnology* **7**, 699–712 (2012).

[12] Li, T. & Galli, G. Electronic properties of mos2 nanoparticles. *The Journal of Physical Chemistry C* **111**, 16192–16196 (2007).

[13] RamakrishnaMatte, H. *et al.* Mos2 and ws2 analogues of graphene. *Angewandte Chemie International Edition* **49**, 4059–4062 (2010).

[14] Splendiani, A. *et al.* Emerging photoluminescence in monolayer mos2. *Nano Letters* **10**, 1271–1275 (2010).

[15] Lopez-Sanchez, O., Lembke, D., Kayci, M., Radenovic, A. & Kis, A. Ultrasensitive photodetectors based on monolayer mos2. *Nature Nanotechnology* **8**, 497–501 (2013).

[16] Tyulnev, I. *et al.* Valleytronics in bulk mos2 with a topologic optical field. *Nature* **628**, 746–751 (2024).

[17] Mai, C. *et al.* Many-body effects in valleytronics: Direct measurement of valley lifetimes in single-layer mos2. *Nano Letters* **14**, 202–206 (2014).

[18] Chan, C.-W., Hsieh, C.-Y., Chan, F.-M., Huang, P.-J. & Yang, C.-Y. Valley Spin-Polarization of MoS(2) monolayer induced by ferromagnetic order in an antiferromagnet. *Materials (Basel)* **17** (2024).

[19] Luo, Y. K. *et al.* Opto-valleytronic spin injection in monolayer mos2/few-layer graphene hybrid spin valves. *Nano Letters* **17**, 3877–3883 (2017).

[20] Liu, R. *et al.* Piezotronic spin and valley transistors based on monolayer mos2. *Nano Energy* **72**, 104678 (2020).

[21] Wu, Y., Li, D., Wu, C.-L., Hwang, H. Y. & Cui, Y. Electrostatic gating and intercalation in 2d materials. *Nature Reviews Materials* **8**, 41–53 (2023).

[22] Tan, Q. *et al.* Layer-dependent correlated phases in wse2/mos2 moiré superlattice. *Nature Materials* **22**, 605–611 (2023).

[23] Novoselov, K. S. *et al.* Two-dimensional gas of massless dirac fermions in graphene. *Nature* **438**, 197–200 (2005).

[24] Zeng, Y. *et al.* Gate-tunable topological phases in superlattice modulated bilayer graphene. *Phys. Rev. B* **109**, 195406 (2024).

[25] Shi, L.-k., Ma, J. & Song, J. C. W. Gate-tunable flat bands in van der waals patterned dielectric superlattices. *2D Materials* **7**, 015028 (2019).

[26] Forsythe, C. *et al.* Band structure engineering of 2d materials using patterned dielectric superlattices. *Nature Nanotechnology* **13**, 566–571 (2018).

[27] Kim, D. S. *et al.* Electrostatic moiré potential from twisted hexagonal boron nitride layers. *Nature Materials* **23**, 65–70 (2024).

[28] He, K., Poole, C., Mak, K. F. & Shan, J. Experimental demonstration of continuous electronic structure tuning via strain in atomically thin mos2. *Nano Letters* **13**, 2931–2936 (2013).

[29] Chen, F. *et al.* Conduction band structure and electron mobility in uniaxially strained si via externally applied strain in nanomembranes. *Journal of Physics D: Applied Physics* **44**, 325107 (2011).

[30] Fischetti, M. V. & Laux, S. E. Band structure, deformation potentials, and carrier mobility in strained si, ge, and sige alloys. *Journal of Applied Physics* **80**, 2234–2252 (1996).

[31] Kourmoulakis, G. *et al.* Strain distribution in ws2 monolayers detected through polarization-resolved second harmonic generation. *Scientific Reports* **14**, 15159 (2024).

[32] Quereda, J., Palacios, J. J., Agräit, N., Castellanos-Gomez, A. & Rubio-Bollinger, G. Strain engineering of schottky barriers in single- and few-layer mos2 vertical devices. *2d materials* **4** (2017).

[33] Zhang, Y. *et al.* Patternable process-induced strain in 2d monolayers and heterobilayers. *ACS Nano* **18**, 4205–4215 (2024). PMID: 38266246.

[34] Henríquez-Guerra, E. *et al.* Modulation of the superconducting phase transition in multilayer 2h-nbse2 induced by uniform biaxial compressive strain. *Nano Letters* **24**, 10504–10509 (2024). PMID: 39075987.

[35] Lu, K. *et al.* Strong second-harmonic generation by sublattice polarization in non-uniformly strained monolayer graphene. *Nature Communications* **14**, 2580 (2023).

[36] Neumann, C. *et al.* Raman spectroscopy as probe of nanometre-scale strain variations in graphene. *Nature Communications* **6**, 8429 (2015).

[37] Deng, S., Che, S., Debbarma, R. & Berry, V. Strain in a single wrinkle on an mos2 flake for in-plane realignment of band structure for enhanced photoresponse. *Nanoscale* **11**, 504–511 (2019).

[38] Tan, C. *et al.* Raman studies of mos2 under strain at different uniaxial directions. *Vacuum* **153**, 274–276 (2018).

[39] Pereira, V. M. & Castro Neto, A. H. Strain engineering of graphene's electronic structure. *Phys. Rev. Lett.* **103**, 046801 (2009).

[40] Bastonero, L., Cicero, G., Palummo, M. & Re Fiorentin, M. Boosted solar light absorbance in pds2/pts2 vertical heterostructures for ultrathin photovoltaic devices. *ACS Applied Materials & Interfaces* **13**, 43615–43621 (2021).

[41] Kayal, A. *et al.* Mobility enhancement in cvd-grown monolayer mos2 via patterned substrate-induced nonuniform straining. *Nano Letters* **23**, 6629–6636 (2023). PMID: 37347123.

[42] Mohiuddin, T. M. G. *et al.* Uniaxial strain in graphene by raman spectroscopy: *g* peak splitting, grüneisen parameters, and sample orientation. *Phys. Rev. B* **79**, 205433 (2009).

[43] Pető, J. *et al.* Moderate strain induced indirect bandgap and conduction electrons in mos2 single layers. *npj 2D Materials and Applications* **3** (2019).

[44] Kang, D.-H. *et al.* Pseudo-magnetic field-induced slow carrier dynamics in periodically strained graphene. *Nature Communications* **12**, 5087 (2021).

[45] Gill, S. T. *et al.* Mechanical control of graphene on engineered pyramidal strain arrays. *ACS Nano* **9**, 5799–5806 (2015).

[46] Hsu, C.-C., Teague, M. L., Wang, J.-Q. & Yeh, N.-C. Nanoscale strain engineering of giant pseudo-magnetic fields, valley polarization, and topological channels in graphene. *Science Advances* **6**, eaat9488 (2020).

[47] Xu, B. *et al.* Switching of the magnetic anisotropy via strain in two dimensional multiferroic materials: Crsx (x=cl, br, i). *Applied Physics Letters* **116**, 052403 (2020).

[48] Xu, X., Liang, T., Kong, D., Wang, B. & Zhi, L. Strain engineering of two-dimensional materials for advanced electrocatalysts. *Materials Today Nano* **14**, 100111 (2021).

[49] Xiong, P. *et al.* Strain engineering of two-dimensional multilayered heterostructures for beyond-lithium-based rechargeable batteries. *Nature Communications* **11**, 3297 (2020).

[50] Feng, J., Qian, X., Huang, C.-W. & Li, J. Strain-engineered artificial atom as a broad-spectrum solar energy funnel. *Nature Photonics* **6**, 866–872 (2012).

[51] Parto, K., Azzam, S. I., Banerjee, K. & Moody, G. Defect and strain engineering of monolayer wse2 enables site-controlled single-photon emission up to 150 k. *Nature Communications* **12**, 3585 (2021).

[52] Xu, X. *et al.* Creating quantum emitters in hexagonal boron nitride deterministically on chip-compatible substrates. *Nano Letters* **21**, 8182–8189 (2021).

[53] Darlington, T. P. *et al.* Imaging strain-localized excitons in nanoscale bubbles of monolayer wse2 at room temperature. *Nature Nanotechnology* **15**, 854–860 (2020).

[54] Mauro, L., Rodríguez-Mena, E. A., Martinez, B. & Niquet, Y.-M. Strain engineering in Ge/Ge−Si spin-qubit heterostructures. *Phys. Rev. Appl.* **23**, 024057 (2025).

[55] Lee, Y. *et al.* Spin-defect qubits in two-dimensional transition metal dichalcogenides operating at telecom wavelengths. *Nature Communications* **13**, 7501 (2022).

[56] Xu, F., Chou, P.-H., Chung, C.-H., Lee, T.-K. & Mou, C.-Y. Strain-induced superconducting pair density wave states in graphene. *Phys. Rev. B* **98**, 205103 (2018).

[57] Celebonovic, V., Pesic, J., Gajic, R., Vasic, B. & Matkovic, A. Selected transport, vibrational, and mechanical properties of low-dimensional systems under strain. *Journal of Applied Physics* **125**, 154301 (2019).

[58] Uchida, M., Nomoto, T., Musashi, M., Arita, R. & Kawasaki, M. Superconductivity in uniquely strained ruo_2 films. *Phys. Rev. Lett.* **125**, 147001 (2020).

[59] Conley, H. J. *et al.* Bandgap engineering of strained monolayer and bilayer mos2. *Nano Letters* **13**, 3626–3630 (2013).

[60] Ali, S. A. *et al.* Room temperature polarization-resolved raman and photoluminescence in uniaxially strained layered mos2. *Applied Physics Letters* **125**, 231902 (2024).

[61] Dadgar, A. M. *et al.* Strain engineering and raman spectroscopy of monolayer transition metal dichalcogenides. *Chemistry of Materials* **30**, 5148–5155 (2018).

[62] Guo, Y. *et al.* Direct bandgap engineering with local biaxial strain in few-layer mos2 bubbles. *Nano Research* **13**, 2072–2078 (2020).

[63] Khestanova, E., Guinea, F., Fumagalli, L., Geim, A. K. & Grigorieva, I. V. Universal shape and pressure inside bubbles appearing in van der waals heterostructures. *Nature Communications* **7**, 12587 (2016).

[64] Hallam, T., Berner, N. C., Yim, C. & Duesberg, G. S. Strain, bubbles, dirt, and folds: A study of graphene polymer-assisted transfer. *Advanced Materials Interfaces* **1**, 1400115 (2014).

[65] Lloyd, D. *et al.* Band gap engineering with ultralarge biaxial strains in suspended monolayer mos2. *Nano Letters* **16**, 5836–5841 (2016).

[66] Yu, Y. *et al.* Engineering substrate interactions for high luminescence efficiency of transition-metal dichalcogenide monolayers. *Advanced Functional Materials* **26**, 4733–4739 (2016).

[67] Martella, C. *et al.* Anisotropic mos2 nanosheets grown on self-organized nanopatterned substrates. *Advanced Materials* **29**, 1605785 (2017).

[68] Liu, B. *et al.* Strain-engineered van der waals interfaces of mixed-dimensional heterostructure arrays. *ACS Nano* **13**, 9057–9066 (2019).

[69] Carpick, R. W. & Salmeron, M. Scratching the surface: fundamental investigations of tribology with atomic force microscopy. *Chemical Reviews* **97**, 1163–1194 (1997).

[70] Ghosh, S., Chandra Karmaker, S., Harish, S. & Saha, B. B. Atomic force microscopic investigations of mos2 thin films produced by low pressure sulfurization. *Micro and Nanostructures* **170**, 207400 (2022).

[71] Giessibl, F. J. Advances in atomic force microscopy. *Rev. Mod. Phys.* **75**, 949–983 (2003).

[72] Li, H. *et al.* From bulk to monolayer mos2: Evolution of raman scattering. *Advanced Functional Materials* **22**, 1385–1390 (2012).

[73] Lee, C. *et al.* Anomalous lattice vibrations of single- and few-layer mos2. *ACS Nano* **4**, 2695–2700 (2010).

[74] O'Brien, M., Scheuschner, N., Maultzsch, J., Duesberg, G. S. & McEvoy, N. Raman spectroscopy of suspended mos2. *physica status solidi (b)* **254**, 1700218 (2017).

[75] Du, G. *et al.* Interlayer engineering of lattice dynamics and elastic constants of 2d layered nanomaterials under pressure. *Nature Communications* **16**, 4901 (2025).

[76] Ferrari, A. C. & Basko, D. M. Raman spectroscopy as a versatile tool for studying the properties of graphene. *Nature Nanotechnology* **8**, 235–246 (2013).

[77] Rao, R. *et al.* Spectroscopic evaluation of charge-transfer doping and strain in graphene/mos_2 heterostructures. *Phys. Rev. B* **99**, 195401 (2019).

[78] Lei, S. *et al.* Surface functionalization of two-dimensional metal chalcogenides by lewis acid–base chemistry. *Nature Nanotechnology* **11**, 465–471 (2016).

[79] Jorio, A., Saito, R., Dresselhaus, G. & Dresselhaus, M. S. Raman spectroscopy in graphene related systems. *WILEY-VCH Verlag GmbH Co. KGaA, Weinheim* (2011).

[80] Verble, J. L. & Wieting, T. J. Lattice mode degeneracy in mos_2 and other layer compounds. *Phys. Rev. Lett.* **25**, 362–365 (1970).

[81] Molina-Sanchez, A. & Wirtz, L. Phonons in single-layer and few-layer mos_2 and ws_2. *Phys. Rev. B* **84**, 155413 (2011).

[82] Molina-Sánchez, A., Hummer, K. & Wirtz, L. Vibrational and optical properties of mos2: From monolayer to bulk. *Surface Science Reports* **70**, 554–586 (2015).

[83] Ding, Y. *et al.* Raman tensor of layered mos2. *Optics Letters* **45**, 1313–1316 (2020).

[84] Ali, S. A. *et al.* Room temperature polarization-resolved raman and photoluminescence in uniaxially strained layered mos2. *Applied Physics Letters* **125**, 231902 (2024).

[85] Sah, R. K., Tang, H., Shahi, C., Ruzsinszky, A. & Perdew, J. P. Effect of strain on the band gap of monolayer mos_2. *Phys. Rev. B* **110**, 144109 (2024).

[86] Franssila, S. Introduction to microfabrication. *John Wiley Sons* (2010).

[87] Electronic Materials Microelectronic technologies, Rohm and Haas. *MEGAPOSIT™ SPR™ 955-CM SERIES PHOTORESIST* (2006). Rev. 0.

[88] Chmielowiec, A., Woś, W. & Gumieniak, J. Viscosity approximation of pdms using weibull function. *Materials* **14** (2021).

[89] Pollack, E. *et al.* Raman spectroscopy of 2d mos2 on ti3c2 mxene: the substrate effect. *Nanoscale Adv.* **7**, 3456–3461 (2025).

[90] Rice, C. *et al.* Raman-scattering measurements and first-principles calculations of strain-induced phonon shifts in monolayer mos_2. *Phys. Rev. B* **87**, 081307 (2013).

[91] Goldie, S. J., Bush, S., Cumming, J. A. & Coleman, K. S. A statistical approach to raman analysis of graphene-related materials: Implications for quality control. *ACS Applied Nano Materials* **3**, 11229–11239 (2020).

[92] Newville, M., Stensitzki, T., Allen, D. B. & Ingargiola, A. LMFIT: Non-Linear Least-Square Minimization and Curve-Fitting for Python (2014).

[93] Li, X. & Zhu, H. Two-dimensional mos2: Properties, preparation, and applications. *Journal of Materiomics* **1**, 33–44 (2015).

[94] Radatović, B. *et al.* Strain-enhanced large-area monolayer mos2 photodetectors. *ACS Applied Materials & Interfaces* **16**, 15596–15604 (2024).

[95] Xiao, X., Li, Y. & Liu, Z. Graphene commercialization. *Nature Materials* **15**, 697–698 (2016).

[96] Bhimanapati, G. R. *et al.* Recent advances in two-dimensional materials beyond graphene. *ACS Nano* **9**, 11509–11539 (2015).

[97] Chang, H.-Y. *et al.* Large-area monolayer mos2 for flexible low-power rf nanoelectronics in the ghz regime. *Advanced Materials* **28**, 1818–1823 (2016).

[98] Zhu, W. *et al.* Black phosphorus flexible thin film transistors at gighertz frequencies. *Nano Letters* **16**, 2301–2306 (2016).

[99] Akinwande, D. *et al.* Large-area graphene electrodes: Using cvd to facilitate applications in commercial touchscreens, flexible nanoelectronics, and neural interfaces. *Nanotechnology Magazine, IEEE* **9**, 6–14 (2015).

[100] Jiang, D. *et al.* Flexible electronics based on 2d transition metal dichalcogenides. *J. Mater. Chem. A* **10**, 89–121 (2022).

Appendix A

Photomask creation

This Appendix details the GDS file used to commission the photomask used for photolithography. In section 2.1.1, we detailed one small section of the photomask, highlighted in yellow on Figure 23. The features highlighted in blue represent the features in Figure 24. The features highlighted in green represent variations of our established patterns with different geometry parameters (varying spacing and/or feature width). The bottom row of patterns in the green area is a duplicate of the top half, simply covering a slightly larger area, which were manufactured in case the patterns were poorly resolved on the mask. As mentioned before, the fidelity of photolithography heavily relies on good contact between the photomask and the wafer. The large (1 cm^2) square highlighted in pink was used to provide a way to monitor the adhesion with the optical setup of the mask aligner and can be seen in the photograph of the mask in Figure 8. The features in red have uses outside the scope of this project. In total, our photomask was designed to have 128 (2 groups of 4 columns of 16 patterns) patterns, to offer us flexibility during the project.

Figure 24 shows a zoomed in version of the GDS file focused on the region in blue in Figure 23. The four zoomed in geometries in the top left corner correspond to the features highlighted in yellow in Figure 23 and the four geometries in Figure 8. This set

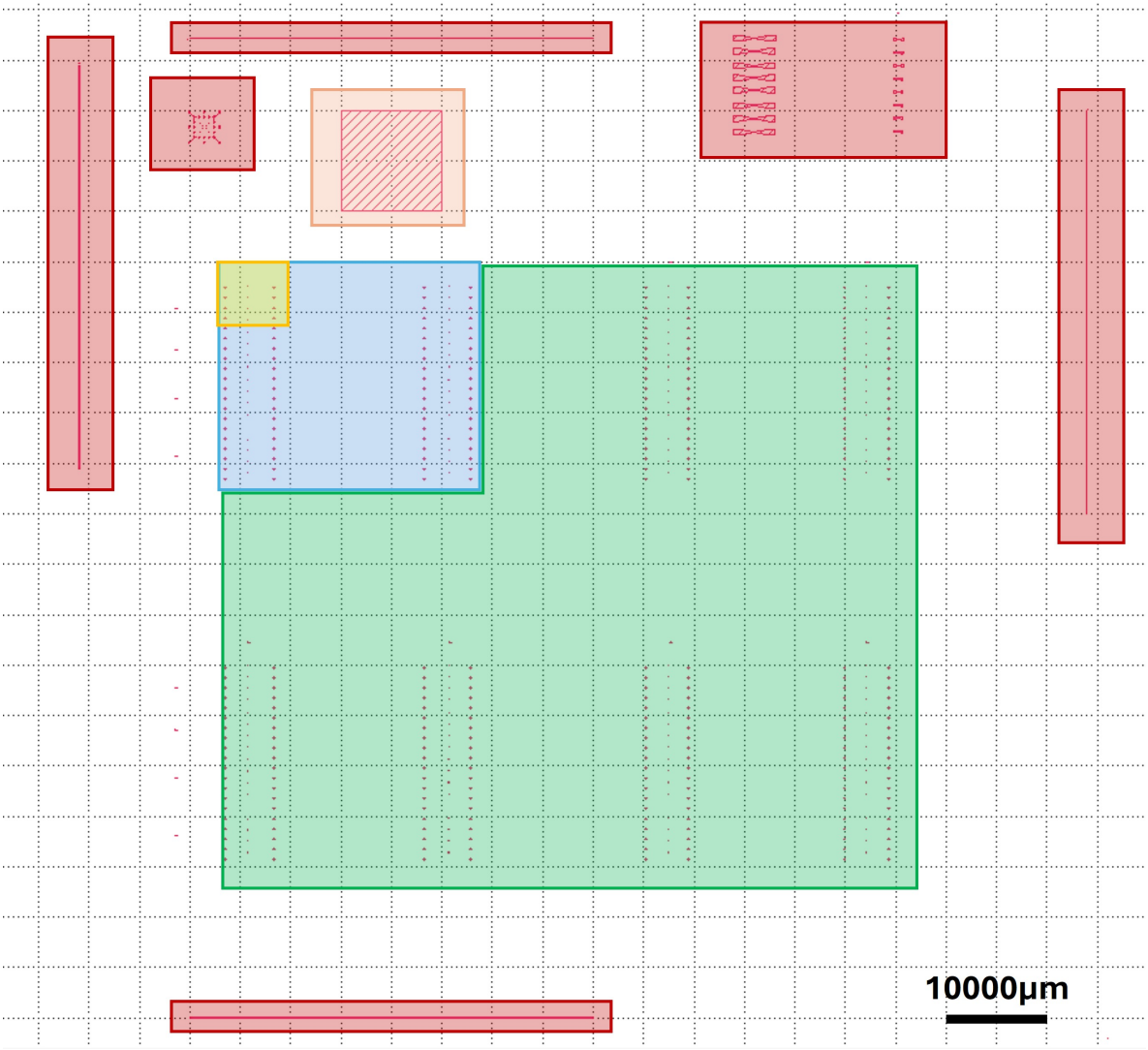

Figure 23: GDS file used for the creation of the photomask

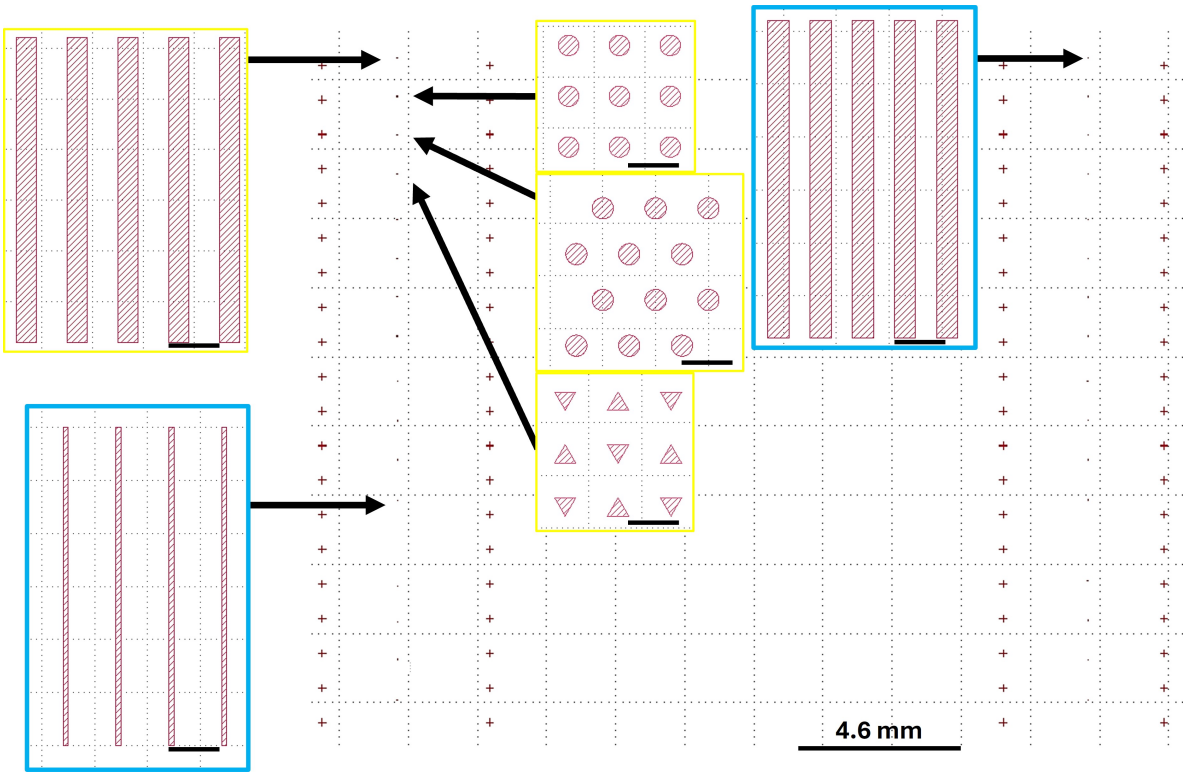

Figure 24: Subset of the GDS file.
This corresponds to the area highlighted in blue in Figure 23.

of 4 patterns repeats 4 times vertically while changing the feature size, which can be seen by the zoomed in bottom left picture showing the pattern of 1D trenches with a feature size of 0.5 μm and the same spacing 2 μm. These columns of 16 patterns are surrounded by alignment marks, which are crosses that help us locate them. Horizontally, we repeated these columns 4 times while changing the spacing: the top right inset shows the pattern of 1D trenches with the same feature size of 2 μm and a spacing of 1.5 μm.

As mentioned in Section 2.1.2, broadening phenomena are not entirely avoidable in photolithography, both during the manufacture of the photomask and during our own lithography processes. Figure 25 shows an example of a pattern with an expected feature size 0.5 μm as it appears on A) the GDS file, B) the photomask, C) one of our photolithography cycles. We observe that broadenings happened at each step, with a

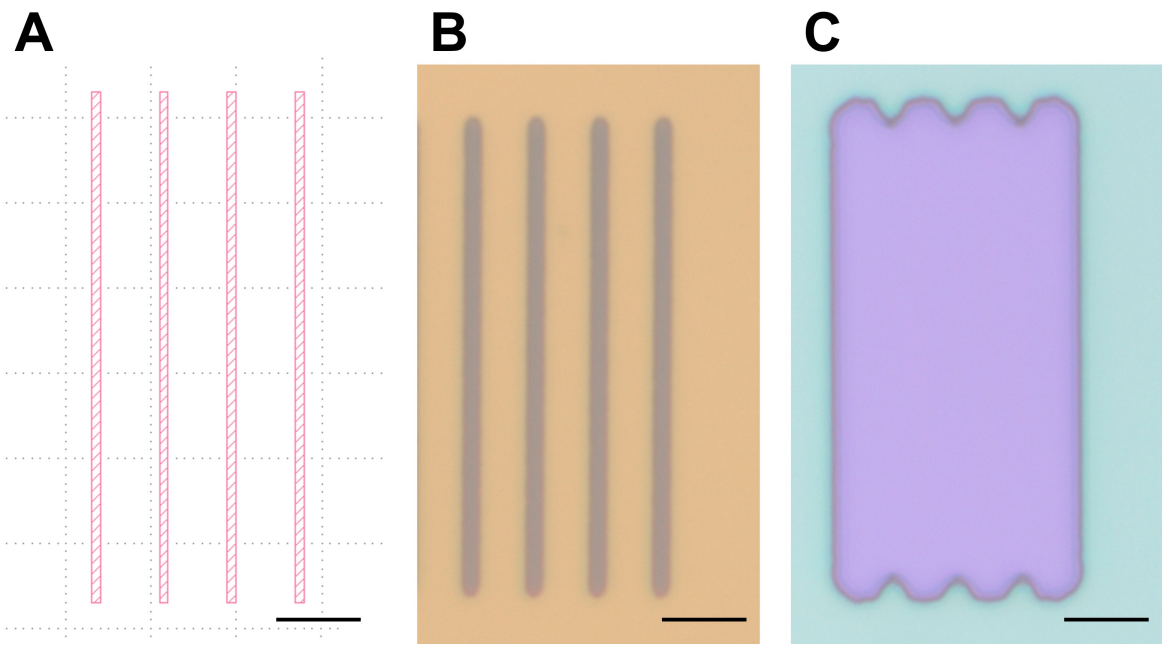

Figure 25: Evolution of a pattern:
A) GDS file, B) on the photomask, C) exposed in the photoresist. This pattern represents a spacing of 4 μm and a feature size of 0.5 μm. All scale bars represent 5 μm.

much more important loss of fidelity in the specific cycle the pattern in Figure 25 C) was a part of.

Appendix B

Exfoliation and Transfer of 2D materials

Depositing a small amount of 2D material onto tape allows to exfoliate it, which is a technique relying on folding that tape onto itself many times to thin down the materials enough to obtain single or few-layers 2D materials. Figure 26 shows the procedure to thin down MoS_2. Steps B) and C) are repeated as many times as necessary to thin down the flakes with the risk of making them hard to pick-up if the steps are repeated too much.

Once the 2D materials exfoliated, different techniques are used to transfer them onto the desired substrates. 2D materials require a precise transfer setup to assemble them together. our transfer setup is shown in Figure B

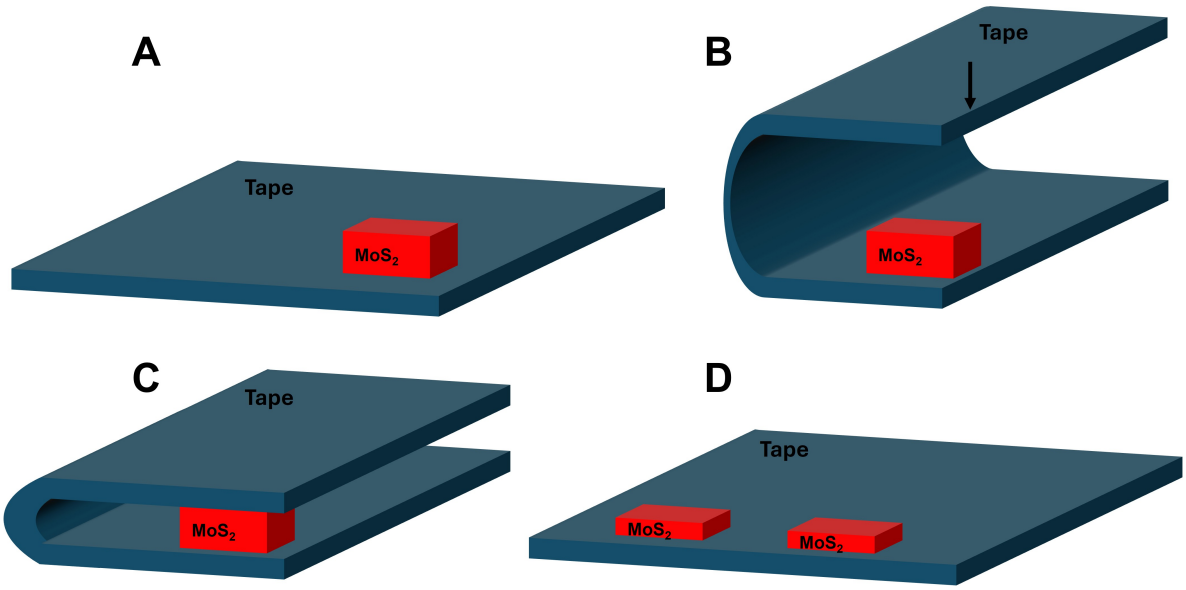

Figure 26: Procedure to obtain thin flakes of 2D material, here MoS_2.
A) Transfer flakes of MoS_2 onto tape. B) Fold the tape onto itself. C) Press tape onto itself. D) Separate the tape.

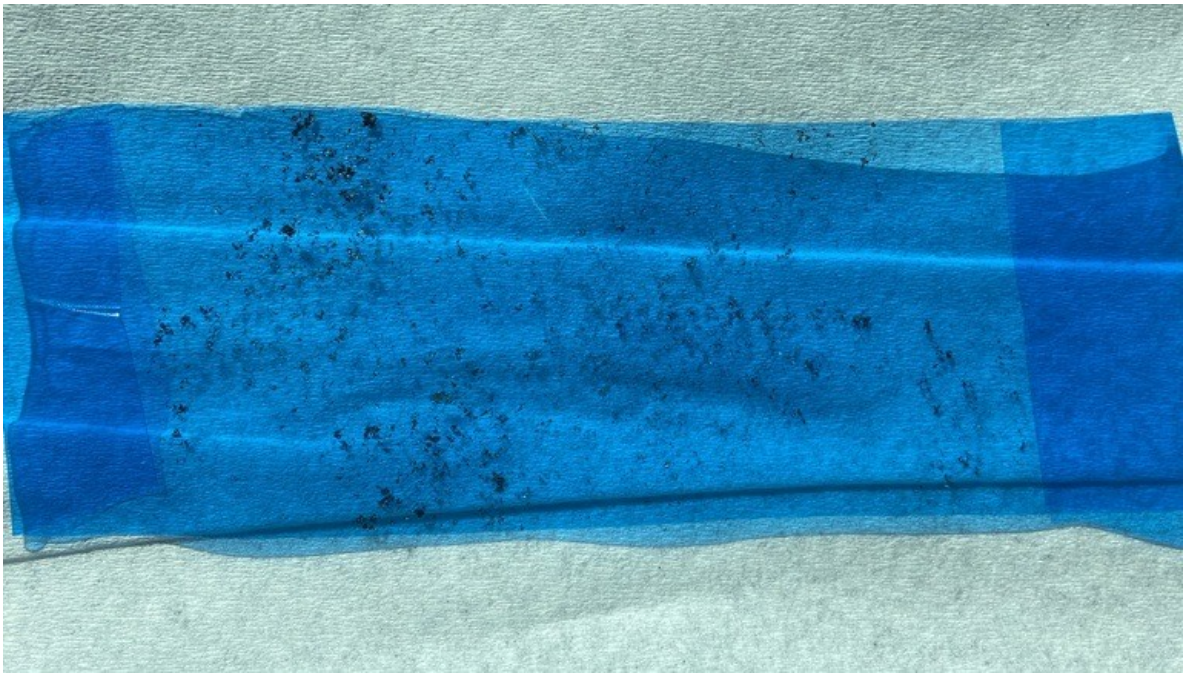

Figure 27: Image of the tape exfoliation, corresponding to step D of Figure 26

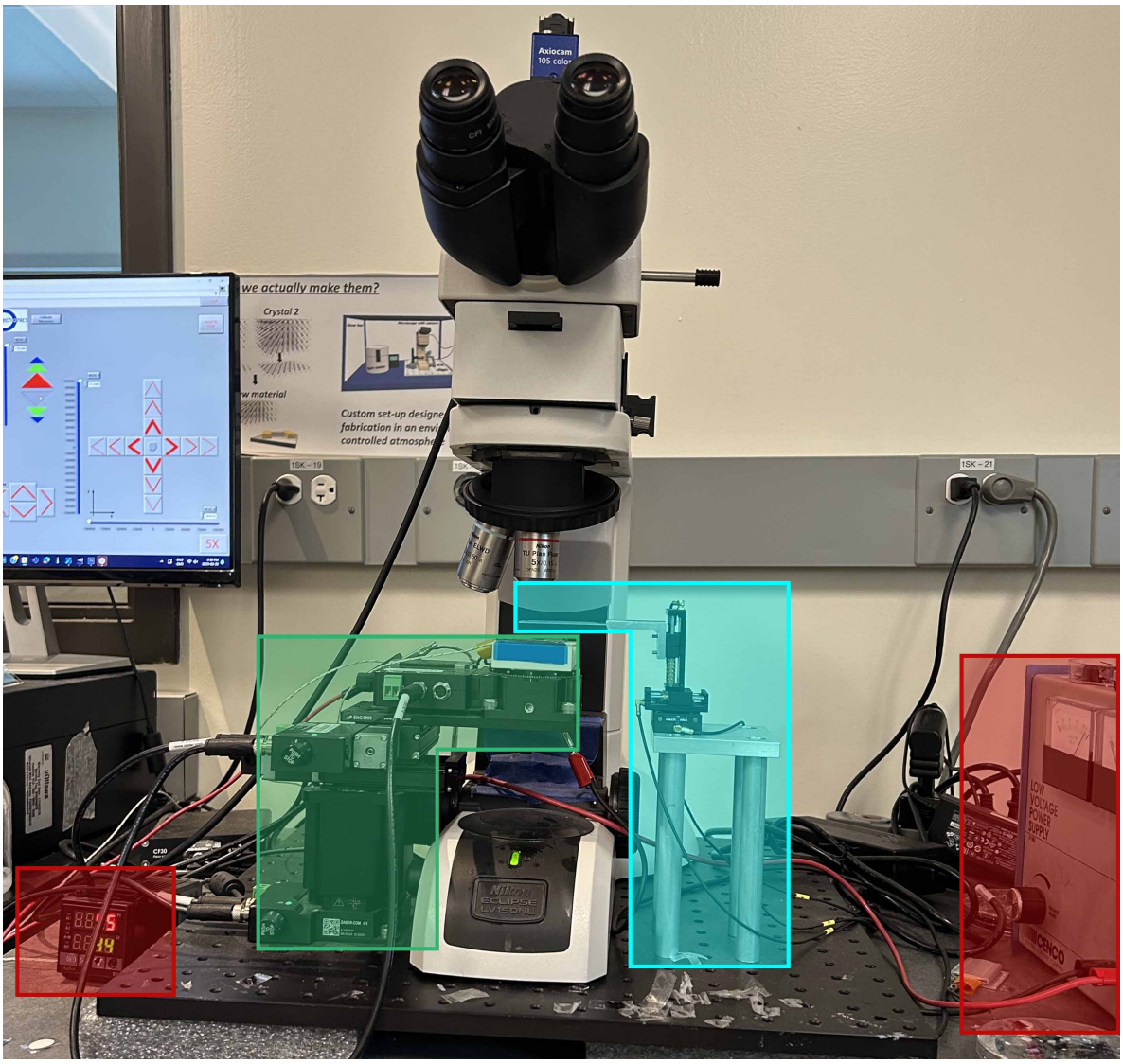

2D material transfer station. Piezoelectric motors control the stage (in green) allowing for precise movement of the substrates. Flakes of 2D materials can be picked up and dropped off with stamps made from spin-coated polymers on glass slides supported by the right manipulator (in blue). Stage temperature can be controlled by a thermocouple (in red). A LV150N optical microscope allows for continuous monitoring of the assembly procedure.

Appendix C

Raman fitting and visualization

```
#This code extracts data from Raman datasets, fits each dataset to two Lorentzians
 ·  and displays spatial maps of the evolution of the Raman modes.

import matplotlib.pyplot as plt
import numpy as np
from lmfit.models import LorentzianModel
from lmfit.models import LinearModel
import seaborn as sns
import pandas as pd
from matplotlib.patches import Rectangle

#Data acquisition
filename = 'Raman map'
filepath = fr'C:\Users\alexandre\Desktop\{filename}.txt'
data = np.loadtxt(filepath, skiprows=52)
wavenumber = data[0, 2:] #The first line of data contains the different wavenumbers
 ·  data was collected at (in cm^-1) .
y_positions = np.round(data[1:, 0],2) #Y position of laser
x_positions = np.round(data[1:, 1],2) #X position of laser
intensity_values = data[1:, 2:] #Signal intensity (in a.u)
```

```
x_positions = np.round(x_positions - np.min(x_positions),2)
y_positions = np.round(y_positions - np.min(y_positions),2)

#Fitting function
def lorentzian(A,s,c,x): #plot Lorentzian from fitted parameters
    result = A*s/(np.pi*((x-c)**2 +s**2))
    return result

Model = LorentzianModel(prefix='l1_') #LMFit allows for composite models: here, we
 . have 2 Lorentzian and 1 linear (background) components
Model+= LorentzianModel(prefix='l2_')
Model+= LinearModel(prefix='bkg_')

[min_x, max_x] = [350, 450] # Spectral range of interest
xfit = np.linspace(min_x, max_x, 1000)
yfit_array = np.ones((len(x_positions), len(xfit))) #Empty arrays to save calculated
 . values
Peak_position = np.ones((len(x_positions), 2))
FWHM = np.ones((len(x_positions), 2))
Stder = np.ones((len(x_positions), 2))

def fitting_function(center1, center2):
    for i in range(len(x_positions)):
        [min_bound1, max_bound1] =[center1 - 8, center1 + 8] #Helps the model find
         . the peak
        [min_bound2, max_bound2] =[ center2 - 8, center2 + 8]
        intensity_values[i,:] = intensity_values[i,:]/ np.max(intensity_values[i,:])
         . #normalize each dataset such that maximum =1
        if np.min(intensity_values[i]) < 0.35: #Ignores datasets on lone SiO2
            params = Model.make_params()
            params['l1_center'].set(value=center1, min=min_bound1, max=max_bound1)
            params['l2_center'].set(value=center2, min=min_bound2, max=max_bound2)
            result = Model.fit(intensity_values[i], params, x=wavenumber)
```

```
if result.params['l1_center'].value < result.params['l2_center'].value:
#this if statement (and the following else) interchang the first and
 · second peak if the model swaps them.
    Peak_position[i][0] = result.params['l1_center'].value
    Peak_position[i][1] = result.params['l2_center'].value
    FWHM[i][0] =  result.params['l1_fwhm'].value
    FWHM[i][1] =  result.params['l2_fwhm'].value
    Stder[i][0] = result.params['l1_center'].stderr
    Stder[i][1] = result.params['l2_center'].stderr
else:
    Peak_position[i][1] = result.params['l1_center'].value
    Peak_position[i][0] = result.params['l2_center'].value
    FWHM[i][1] =  result.params['l1_fwhm'].value
    FWHM[i][0] =  result.params['l2_fwhm'].value
    Stder[i][1] = result.params['l1_center'].stderr
    Stder[i][0] = result.params['l2_center'].stderr

if np.max(intensity_values[i,:]) <= 0.3 +
 · np.median(intensity_values[i,:]) or result.params['l2_fwhm'].value >
 · 15 or result.params['l1_fwhm'].value > 10 or
 · result.params['l2_fwhm'].value < 3 or result.params['l1_fwhm'].value
 · < 3 or result.params['l1_amplitude'].value < 0.1 or
 · result.params['l2_amplitude'].value < 0.1: #if any of these
 · conditions are met (which datasets taken on lone SiO2 do), then save
 · easily identifiable values.
    Peak_position[i][0] = 1
    Peak_position[i][1] = 1
    FWHM[i][0] = 1
    FWHM[i][1] = 1
    Stder[i][0] = 25
    Stder[i][1] = 25

yfit = lorentzian(result.params['l1_amplitude'].value,
 · result.params['l1_sigma'].value, result.params['l1_center'].value,
 · xfit) #Use the calculated parameters to obtain the fitted curve
```

```
            yfit += lorentzian(result.params['l2_amplitude'].value,
             · result.params['l2_sigma'].value, result.params['l2_center'].value,
             · xfit)
            yfit += result.params['bkg_slope'].value * xfit +
             · result.params['bkg_intercept'].value
            print(Peak_position[i,:])
            yfit_array[i, :] = yfit #save the fitted curve

fitting_function(382, 407) #initial guesses influence the model


# This next piece of code displays the value of the peak positions for each set of x
 · and y coordinates. The results are the heatmaps seen in Figures 14 C), D) and E)
 · and 15 D), E), F).

def heatmap(data, title, cbar_bounds, color_guide):
    df = pd.DataFrame({'Peak Position': data, 'x': x_positions, 'y': y_positions})
    heatmap_data = df.pivot(index='y', columns='x', values='Peak Position')
    plt.figure(figsize=(11, 8))
    ax = sns.heatmap(heatmap_data, annot=False, vmin=cbar_bounds[0],
     · vmax=cbar_bounds[1], square=False, cmap=color_guide) #heatmap function
    ax.set_aspect("equal")

    for y in range(heatmap_data.shape[0]): # this for loop covers all datasets on
     · lone SiO2 (identified by a value of Peak position of 1) by a black square
        for x in range(heatmap_data.shape[1]):
            if heatmap_data.iloc[y, x] == 1 or heatmap_data.iloc[y, x] == 0:
                ax.add_patch(plt.Rectangle((x, y), 1, 1, color='black', ec='black'))

    cbar = ax.collections[0].colorbar
    pos = ax.get_position()
    cbar.ax.set_position([pos.x1 + 0.03, pos.y0, 0.04, pos.height]) #Set the
     · colorbar parameters
    cbar.set_ticks(np.linspace(cbar_bounds[0], cbar_bounds[1], num=6))
```

```
    cbar.ax.set_yticklabels([f"{tick:.1f}" for tick in cbar.get_ticks()],
     · fontsize=20)
    plt.xticks(ticks=plt.xticks()[0][::3], fontsize=17.5, rotation=0)
    plt.yticks(ticks=plt.yticks()[0][::3], fontsize=17.5, rotation=0)
    plt.xlabel("x [m]", fontsize=25)
    plt.ylabel("y [m]", fontsize=25)
    plt.title(fr"{title} peak positions", fontsize=25)
    plt.show()
    return heatmap_data

def color_bounds(index):
    color_bound1 = np.min(Peak_position[Peak_position[:,index] > 5, index]) #Sets
     · the minimum colorbar value to be the lowest Peak position value that isn't 1
     · (Hence why we set the peak position value of the datasets on lone SiO2 to 1
     · )
    color_bound2 = np.max(Peak_position[Peak_position[:,index] > 5, index])
    return(color_bound1, color_bound2)

heatmap_E12g = heatmap(Peak_position[:,0], 'E$^1_{2g}$', color_bounds(0), "Greens")
heatmap_A1g = heatmap(Peak_position[:,1], 'A$_{1g}$', color_bounds(1), "Reds")
Peak_difference = Peak_position[:,1] - Peak_position[:,0]
heatmap_diff = heatmap(Peak_difference, 'A$_{1g} - E^1_{2g}$',
 · [np.min(Peak_difference[Peak_difference>17]),np.max(Peak_difference)], "YlGnBu")


#This next function shows the evolution of the peak positions values at specific x
 · positions, averaged with their 2 nearest same-column neighbours. The results are
 · the plots shown in Figure 15 G), H) and I)


def Peak_position_averages(df, title, y_value, x_min_1, x_max_1, x_min_2, x_max_2,
 · Stder, color):
    yerr = (wavenumber[-1] - wavenumber[0])/(2*len(wavenumber)) #Y uncertainty comes
     · from spectral step size
```

```
y_vals = df.index.values
x_vals = df.columns.values
pos = np.where(y_vals == y_value)[0][0]
x_mask_1 = (x_vals >= x_min_1) & (x_vals <= x_max_1) # Define masks to only show
 · (in this case, 3) datasets, centered around the one that we are interested
 · in
x_mask_2 = (x_vals >= x_min_2) & (x_vals <= x_max_2)
raw_1 = df.loc[y_vals[pos]].values[x_mask_1] #corresponds to the 5 values
 · directly along y_value, within the x bounds imposed by x_mask.
raw_2 = df.loc[y_vals[pos]].values[x_mask_2]
avg_1 = (raw_1 + df.loc[y_vals[pos+1]].values[x_mask_1] +
 · df.loc[y_vals[pos-1]].values[x_mask_1]) /3 #average with directly above and
 · below neighbours
avg_2 = (raw_2 + df.loc[y_vals[pos+1]].values[x_mask_2] +
 · df.loc[y_vals[pos-1]].values[x_mask_2]) /3

fig, (ax1, ax2) = plt.subplots(1, 2, sharey=True, figsize=(12, 6),
 · gridspec_kw={'wspace': 0.05})

e1a = ax1.errorbar(x_vals[x_mask_1], avg_1, yerr= yerr, xerr=0.25, fmt='o',
 · label='Averaged', capsize=4, color=color)
e1a[-1][0].set_linestyle('--')
e1a[-1][1].set_linestyle('--')
ax1.set_xlim(x_min_1 - 0.27, x_max_1 + 0.15)
ax1.set_xlabel("x [m]", fontsize=16)
ax1.set_ylabel(r'Wavenumber [cm$^{-1}$]', fontsize=16)
ax1.set_xticks(x_vals[x_mask_1])
ax1.set_xticklabels([f"{val:.2f}" for val in x_vals[x_mask_1]])
ax1.tick_params(axis='both', labelsize=18)

e2a = ax2.errorbar(x_vals[x_mask_2], avg_2, yerr= yerr, xerr=0.25, fmt='o',
 · label='Averaged', capsize=4, color=color)
e2a[-1][0].set_linestyle('--')
e2a[-1][1].set_linestyle('--')
```

```
    ax2.set_xlim(x_min_2 - 0.2, x_max_2 + 0.27)
    ax2.set_xticks(x_vals[x_mask_2])
    ax2.set_xticklabels([f"{val:.2f}" for val in x_vals[x_mask_2]])
    ax2.tick_params(axis='both', labelsize=18)


    ax2.set_xlabel("x [m]", fontsize=16)

    kwargs = dict(transform=ax1.transAxes, color='k', clip_on=False)
    ax1.plot((1,1) , (0,0), **kwargs)
    ax1.plot((1, 1), (1, 1), **kwargs)
    kwargs.update(transform=ax2.transAxes)
    ax2.plot((0,0), (0,0), **kwargs)
    ax2.plot((0,0), (1, 1), **kwargs)
    plt.suptitle(fr'Evolution of {title} at y = {y_value}', fontsize=20)
    plt.show()


Peak_position_averages(heatmap_E12g, 'E$^1_{2g}$',  4.47 , 3.45, 5.1, 6.1, 7.7,
 · Stder, 'green') #This command displays the evolution of the E12g peak position
 · on the line corresponding to y_position=4.47,avergaed with its 2 nearest
 · same-column neighbours, for x_positions between 3.45 and 5.1, as well as between
 · 6.1 and 7.7.
Peak_position_averages(heatmap_A1g, 'A$_{1g}$',  4.47 , 3.45, 5.1, 6.1, 7.7, Stder,
 · 'red')
Peak_position_averages(heatmap_diff, 'A$_{1g} - E^1_{2g}$',  4.47 , 3.45, 5.1, 6.1,
 · 7.7, Stder, 'blue')
```